Closed-form matrix dynamics of the n-link pendulum: chaos analysis and real-time state estimation

Haydar K. Karhan and Zafer Bingül

Department of Mechatronics Engineering, Kocaeli University, 41001, Kocaeli, Türkiye.

*Corresponding author(s). E-mail(s): zaferb@kocaeli.edu.tr;
Contributing authors: haydar.karhan@kocaeli.edu.tr;

Abstract

Multi-link planar pendulums are a canonical benchmark for nonlinear dynamics. However, as the link count increases, standard recursive formulations become slow, which limits their use in chaos analysis and real-time state estimation. We derive a closed-form matrix representation of the n-link planar pendulum dynamics in absolute generalized coordinates, built from diagonal sine and cosine matrices and a constant coupling matrix, together with the analytical continuous-time Jacobian of the full state transition. Within the range of 1 to 40 links, the forward dynamics exhibits empirical scaling with exponent 0.97 against 2.06 for an iterative reference, and the analytical Jacobian agrees with a central-difference reference to a relative Frobenius-norm error below one part in a billion at 15 links. A systematic chaos analysis across link counts from 1 to 12 combines recurrence quantification with the full Benettin–QR Lyapunov spectrum and identifies three links as the principal transition into hyperchaos. Experimentally, an Extended Kalman Filter using the analytical Jacobian recovers the full 20-dimensional state of a custom-built 10-link pendulum in real time on a dSPACE MicroAutoBox II at 600 Hz with a mean NRMSE of 1.3%, and a measurement-rate sweep exposes an observability collapse near the Nyquist rate of the dominant linearized mode. These results close the gap between closed-form multi-link dynamics, dimensional chaos thresholds, and real-time state estimation on physical high-degree-of-freedom hardware.

Keywords: n-link pendulum, closed-form matrix dynamics, analytical Jacobian, chaos, multi-rate extended Kalman filter

1 Introduction

Multi-link pendulum systems remain among the most enduring benchmark models in the fields of mechanics, robotics, and control theory. Despite their geometric simplicity, they exhibit underactuation, strong nonlinear coupling, and complex transient and steady-state behaviors that touch nearly every facet of nonlinear dynamics [1, 2]. They serve simultaneously as testbeds for controller design in applications ranging from overhead cranes [3, 4] and bipedal locomotion to robotic manipulators, and as canonical examples through which chaos, bifurcation, and resonance phenomena are studied [5–7]. Therefore, three distinct but interrelated demands have driven

research on these systems: an efficient and analytically tractable model of the dynamics, a quantitative characterization of their chaotic behavior as complexity increases, and a robust state-observation framework capable of operating in real time on physical hardware. The present work addresses these three demands within a single, unified framework.

Mathematical modeling of n-link pendulums has classically been pursued via Lagrangian or Newton–Euler formalisms [8–11]. Many of these derivations adopt relative joint coordinates and rely on recursive iterative algorithms, often in conjunction with the Denavit–Hartenberg convention [12]. Although such formulations are convenient for general-purpose multibody codes, recent studies have shown that the choice of coordinate system has a marked impact on computational efficiency; dynamic equations written in absolute coordinates can be evaluated faster and with smaller integration errors than their relative-coordinate counterparts of comparable fidelity [2]. Variants of the n-link problem have also been examined in coordinate-free [13, 14] and energy-based frameworks for specific trajectories [15], and asymptotic and fractional perspectives have been pursued for limiting cases, such as the hanging-chain pendulum [16] and abstract Ziegler-type extensions [17]. The Udwadia–Koganti formulation [18] further established compact equations of motion via induction. Despite this rich literature, explicit closed-form matrix dynamic equations that avoid the per-step overhead of recursive iteration and simultaneously expose structural properties such as the skew-symmetry of $(\dot{\mathbf{M}} - 2\mathbf{C})$ remain absent. Equally missing is an explicit analytical Jacobian of the n-link pendulum's full state transition, which is indispensable for advanced real-time control optimization and model-based observer design at large n.

Beyond modeling, the inherent nonlinearity of multi-link pendulums renders them excellent testbeds for investigating chaos, bifurcations, and resonance. Order-to-chaos and chaos-to-order transitions have been analyzed across diverse configurations, including spring-mass-spherical pendula [19], damped oscillators coupled with spherical pendula and piezoelectric transducers [20], and triple rigid-body and planar double pendula near resonance [21, 22]. Closer to the present setting, several authors have studied the periodic-to-chaotic route in forced single, double, and triple pendula [17, 23–25]. To quantify the resulting unpredictability, Lyapunov characteristic exponents (LCEs) have become the dominant diagnostic; the variational framework of Benettin et al. [26, 27] together with the QR-based standard method surveyed by Skokos [28] provides direct access to the full spectrum when the dynamics and its Jacobian are available analytically, while time-series–based estimators such as those of Wolf et al. [29] and Rosenstein et al. [30] address the experimental setting in which only scalar observations are accessible. Subsequent refinements [31–35] have improved the efficiency and robustness of these methods, particularly for noisy or moderately dimensional systems. Complementing these scalar diagnostics, recurrence plot (RP) analysis [36, 37] and the associated recurrence quantification analysis (RQA) provide a topological view of the return structure in the phase space and have been applied successfully to identify transitions, fault signatures, and intermittency in single and multi-link pendula [38–41]. However, the vast majority of these chaotic evaluations are confined to simple, double, or triple pendulum models. A systematic, comparative chaos analysis that tracks the joint evolution of recurrence statistics and the full Lyapunov spectrum across a varying and arbitrary number of links—and thereby resolves the dimensional threshold at which hyperchaos emerges—remains a notable gap.

Accurate chaos analysis and control of a physical pendulum are virtually impossible without precise knowledge of the full state of the system, and direct measurement of joint torques or external wrenches is often intrusive, expensive, or impractical for passive lightweight structures [42]. Model-based filtering approaches, such as the Extended Kalman Filter (EKF), Unscented Kalman Filter, and the Error-State Kalman Filter, are routinely deployed to reconstruct kinematics, friction, and unknown torques from limited sensor data [43–46]. Recent work has demonstrated the viability of purely vision-based state tracking on multi-link passive chains [47]. Yet most experimental validations are confined to low-DOF mechanisms or idealized simulations, and the link between the predictability horizon of the underlying chaotic dynamics and the sampling rate for filter convergence has, to our knowledge, not been

demonstrated empirically on a high-DOF physical system.

Motivated by these gaps, this paper develops a unified framework for the modeling, chaos analysis, and real-time state estimation of n-link planar pendulum systems, with four specific contributions:

1. An explicit closed-form matrix representation of the n-link pendulum dynamics in absolute generalized coordinates is derived, in which the mass, Coriolis/centrifugal, and gravity terms are built from diagonal sine/cosine matrices and a constant coupling matrix. The skew-symmetry of $\dot{\mathbf{M}} - 2\mathbf{C}$ is established in closed-form, and the empirical scaling within the operating range $n \in [1, 40]$ is $t \propto n^{0.97}$ against $t \propto n^{2.06}$ for a state-of-the-art iterative reference [2].
2. The analytical continuous-time Jacobian of the full state transition is derived in the same structured operands as the dynamics itself, eliminating both the truncation error and the $\mathcal{O}(n)$ overhead per evaluation incurred by finite-difference linearization.
3. A systematic chaos analysis is performed across $n = 1, \ldots, 12$, combining recurrence quantification with the full Benettin–QR Lyapunov spectrum on a common set of energy-normalized trajectories. The two diagnostics jointly identify $n = 3$ as the principal transition into hyperchaos.
4. The framework is validated experimentally on a custom-built 10-link pendulum tracked at 600 Hz by a motion-capture system, where an Extended Kalman Filter using the analytical Jacobian recovers the full 20-dimensional state from Cartesian markers in real time. Sweeping the measurement rate exposes an observability collapse when the sampling frequency approaches the Nyquist rate of the dominant linearized mode, identifying a lower bound on the measurement frequency for real-time state tracking.

The remainder of this paper is organized as follows. Section 2 establishes the kinematics, friction models, and notations. Section 3 derives the closed-form matrix dynamics, and Section 4 presents the analytical Jacobian, together with numerical correctness and computational performance benchmarks. Section 5 reports the recurrence and Lyapunov analyses across $n = 1, \ldots, 12$. Sections 6 and 7 describe the experimental platform, datasets, and EKF design. Section 8 evaluates the real-time state tracking performance and sampling rate sensitivity. Section 9 concludes the paper and provides directions for future work.

2 System model

The modeling of the n-link pendulum is generally performed using two different generalized coordinates. Relative coordinates are defined as the angles between consecutive links, where the first link is defined with respect to a vertical reference, as shown in Fig. 1(a). The absolute coordinates were defined as the angle of each link with respect to a common reference frame, as shown in Fig. 1(b). In this paper, absolute and relative coordinates are indicated by the symbols $\mathbf{q}$ and $\mathbf{r}$ respectively.

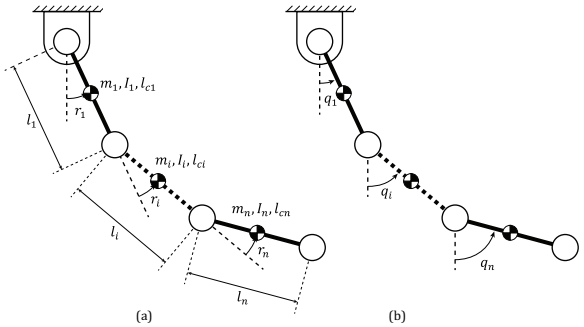


Fig. 1: Schematic of the n-link planar pendulum in (**a**) relative and (**b**) absolute coordinates

The impact of absolute and relative coordinates on computational performance was greatly analyzed in [2].

2.1 Kinematics

In this paper, absolute coordinates were mostly utilized. However, absolute coordinates can be transformed to relative coordinates by using the expression

$$\mathbf{r} = \mathbf{\Phi q} \tag{1}$$

where $\mathbf{\Phi} \in \mathbb{R}^{n\times n}$ is defined as

$$\mathbf{\Phi} = \begin{bmatrix} 1 & 0 & \cdots & 0 & 0 \\ -1 & 1 & \cdots & 0 & 0 \\ \vdots & \vdots & \ddots & \vdots & \vdots \\ 0 & 0 & \cdots & 1 & 0 \\ 0 & 0 & \cdots & -1 & 1 \end{bmatrix}.$$

The matrix $\mathbf{\Phi}$ is invertible because it is triangular and has ones on the diagonal. Thus, the inverse transformation from relative to absolute coordinates can be written as $\mathbf{q} = \mathbf{\Phi}^{-1}\mathbf{r}$.

Consider an n-link chain with link lengths denoted by l_i and the corresponding center of mass (CoM) distance along the link is defined as l_{ci}. Each link has a mass of m_i and a moment of inertia about the CoM of I_i. The index i is $1 \leq i \leq n$. A matrix $\mathbf{\Lambda} \in \mathbb{R}^{n\times n}$ containing the link length parameters is defined as

$$\mathbf{\Lambda} = \begin{bmatrix} l_{c1} & 0 & \cdots & 0 \\ l_1 & l_{c2} & \cdots & 0 \\ \vdots & \vdots & \ddots & \vdots \\ l_1 & l_2 & \cdots & l_{cn} \end{bmatrix}. \tag{2}$$

Furthermore, the vectors $\mathbf{s}(\mathbf{q}), \mathbf{c}(\mathbf{q}) \in \mathbb{R}^n$ are defined as

$$\mathbf{s}(\mathbf{q}) = \begin{bmatrix} \sin(q_1) & \dots & \sin(q_n) \end{bmatrix}^\top \tag{3}$$

$$\mathbf{c}(\mathbf{q}) = \begin{bmatrix} \cos(q_1) & \dots & \cos(q_n) \end{bmatrix}^\top. \tag{4}$$

The x and y positions of each link's respective CoM can thus be written as the stacked vectors

$$\mathbf{x}_c = \mathbf{\Lambda}\,\mathbf{s}(\mathbf{q}) \tag{5}$$

$$\mathbf{y}_c = -\mathbf{\Lambda}\,\mathbf{c}(\mathbf{q}), \tag{6}$$

with their first order time derivatives defined as

$$\dot{\mathbf{x}}_c = \mathbf{\Lambda}\mathbf{D}_c(\mathbf{q})\dot{\mathbf{q}} \tag{7}$$

$$\dot{\mathbf{y}}_c = -\mathbf{\Lambda}\mathbf{D}_s(\mathbf{q})\dot{\mathbf{q}} \tag{8}$$

where the matrices $\mathbf{D}_c(\mathbf{q}) = \mathrm{diag}(\mathbf{c}(\mathbf{q}))$ and $\mathbf{D}_s(\mathbf{q}) = \mathrm{diag}(\mathbf{s}(\mathbf{q}))$.

2.2 Friction

Friction torque is generally defined in relative coordinates. Thus, a transformation between the relative and absolute torques must be defined. Let the friction in the relative coordinates be defined as $\tau_{f,r}(\dot{\mathbf{r}}) \in \mathbb{R}^n$, with $\dot{\mathbf{r}} = \mathbf{\Phi}\dot{\mathbf{q}}$. The friction torque in absolute coordinates is defined as $\tau_{f,q}(\dot{\mathbf{q}}) \in \mathbb{R}^n$. Virtual displacements are defined as $\partial\mathbf{r} = \mathbf{\Phi}\partial\mathbf{q}$. The friction in both relative and absolute coordinates must perform the same virtual work defined by

$$\begin{aligned} \partial W &= \tau_{f,q}^\top \partial\mathbf{q} = \tau_{f,r}^\top \partial\mathbf{r} = \tau_{f,r}^\top \mathbf{\Phi}\partial\mathbf{q} \\ \tau_{f,q}(\dot{\mathbf{q}}) &= \mathbf{\Phi}^\top \tau_{f,r}(\dot{\mathbf{r}}). \end{aligned} \tag{9}$$

Thus, any friction model employed in relative coordinates can be transformed into absolute coordinates using (9).

If each joint is assumed to have a Coulomb and viscous friction model, this yields the friction torque defined in relative coordinates as

$$\tau_{f,r}(\dot{\mathbf{r}}) = -\mathbf{D}_B\dot{\mathbf{r}} - \mathbf{D}_C \tanh(\dot{\mathbf{r}}/\varepsilon) \tag{10}$$

where the matrices $\mathbf{D}_B,\ \mathbf{D}_C \in \mathbb{R}^{n\times n}$ are the viscous and Coulomb friction coefficient diagonal matrices, respectively. The viscous and Coulomb friction coefficients of each joint i are written in the (i,i)'th index. The $\tanh(\cdot)$ function was chosen for its continuous differentiability. The parameter ε is the smoothing operator, which is chosen as $\frac{2}{3}$ throughout the paper.

3 Closed-form dynamics

The Lagrangian of the system can be expressed as

$$L = T - U \tag{11}$$

where T and U denote the kinetic and potential energy of the system, respectively, with

$$\begin{aligned} T &= \frac{1}{2}\left(\dot{\mathbf{x}}^\top\mathbf{D}_m\dot{\mathbf{x}} + \dot{\mathbf{y}}^\top\mathbf{D}_m\dot{\mathbf{y}}\right) + \frac{1}{2}\dot{\mathbf{q}}^\top\mathbf{D}_I\dot{\mathbf{q}} \\ &= \frac{1}{2}\dot{\mathbf{q}}^\top\Big(\mathbf{D}_c\mathbf{W}\mathbf{D}_c + \mathbf{D}_s\mathbf{W}\mathbf{D}_s + \mathbf{D}_I\Big)\dot{\mathbf{q}} \end{aligned} \tag{12}$$

$$U = g\,\mathbf{1}^\top\mathbf{D}_m\mathbf{\Lambda}\big(\mathbf{1} - \mathbf{c}(\mathbf{q})\big) \geq 0 \tag{13}$$

where

$$\mathbf{W} = \mathbf{\Lambda}^\top\mathbf{D}_m\mathbf{\Lambda} \tag{14}$$

$$\mathbf{D}_m = \mathrm{diag}(m_1, \dots, m_n) \tag{15}$$

$$\mathbf{D}_I = \text{diag}(I_1, \ldots, I_n). \tag{16}$$

Note that the potential energy U is minimum when $\mathbf{q} = \mathbf{0}$, and maximum when $\mathbf{q} = \pi$. Using Eqs. (12) and (13), the dynamics are defined as:

$$\frac{d}{dt}\left(\frac{\partial T}{\partial \dot{\mathbf{q}}}\right) - \frac{\partial T}{\partial \mathbf{q}} + \frac{\partial U}{\partial \mathbf{q}} = \tau_{f,q} \tag{17}$$

which evaluates to the general form

$$\mathbf{M}(\mathbf{q})\ddot{\mathbf{q}} + \mathbf{C}(\mathbf{q}, \dot{\mathbf{q}})\dot{\mathbf{q}} + \mathbf{g}(\mathbf{q}) = \tau_{f,q}(\dot{\mathbf{q}}) \tag{18}$$

where the mass matrix and Coriolis and centrifugal force matrix are denoted as $\mathbf{M}$, $\mathbf{C} \in \mathbb{R}^{n\times n}$ respectively. The gravity vector is defined as $\mathbf{g} \in \mathbb{R}^n$. The elements in (18) are defined as follows:

$$\mathbf{M}(\mathbf{q}) = \mathbf{M}_0(\mathbf{q}) + \mathbf{D}_I, \tag{19}$$
$$\mathbf{C}(\mathbf{q}, \dot{\mathbf{q}}) = \mathbf{C}_0(\mathbf{q})\mathbf{D}_\omega(\dot{\mathbf{q}}), \tag{20}$$
$$\mathbf{g}(\mathbf{q}) = g\,\mathbf{D}_s\mathbf{\Lambda}^\top\mathbf{D}_m\mathbf{1}, \tag{21}$$
$$\mathbf{M}_0(\mathbf{q}) = \mathbf{D}_c\mathbf{W}\mathbf{D}_c + \mathbf{D}_s\mathbf{W}\mathbf{D}_s, \tag{22}$$
$$\mathbf{C}_0(\mathbf{q}) = \mathbf{D}_s\mathbf{W}\mathbf{D}_c - \mathbf{D}_c\mathbf{W}\mathbf{D}_s, \tag{23}$$
$$\mathbf{D}_\omega(\dot{\mathbf{q}}) = \text{diag}(\dot{q}_1, \ldots, \dot{q}_n). \tag{24}$$

A standard energy consistency property is that $\dot{\mathbf{M}} - 2\mathbf{C}$ is skew-symmetric, which ensures $\dot{\mathbf{q}}^\top\big(\dot{\mathbf{M}} - 2\mathbf{C}\big)\dot{\mathbf{q}} = 0$. Although different choices for $\mathbf{C}$ can represent the same Coriolis/centrifugal vector, the definition in (20) yields the skew-symmetry property in a closed form.

Lemma 1 Let $\mathbf{C}_0$ be defined in (23). Then, $\mathbf{C}_0$ is skew-symmetric, that is, $\mathbf{C}_0^\top = -\mathbf{C}_0$.

Proof Since $\mathbf{W} = \mathbf{W}^\top$ and $\mathbf{D}_s, \mathbf{D}_c$ are diagonal (hence symmetric), we have

$$\begin{aligned}\mathbf{C}_0^\top &= \big(\mathbf{D}_s\mathbf{W}\mathbf{D}_c - \mathbf{D}_c\mathbf{W}\mathbf{D}_s\big)^\top \\ &= \mathbf{D}_c\mathbf{W}\mathbf{D}_s - \mathbf{D}_s\mathbf{W}\mathbf{D}_c = -\mathbf{C}_0.\end{aligned} \tag{25}$$

□

Lemma 2 Let $\mathbf{M}$ and $\mathbf{C}$ be defined by (19) and (20), respectively. Then

$$\mathbf{K} = \dot{\mathbf{M}} - 2\mathbf{C} \tag{26}$$

is skew-symmetric.

Proof Using $\dot{\mathbf{D}}_c = -\mathbf{D}_s\mathbf{D}_\omega$ and $\dot{\mathbf{D}}_s = \mathbf{D}_c\mathbf{D}_\omega$, and noting that $\mathbf{W}$ and $\mathbf{D}_I$ are constant, differentiation of (19) yields

$$\begin{aligned}\dot{\mathbf{M}} &= \dot{\mathbf{D}}_c\mathbf{W}\mathbf{D}_c + \mathbf{D}_c\mathbf{W}\dot{\mathbf{D}}_c + \dot{\mathbf{D}}_s\mathbf{W}\mathbf{D}_s + \mathbf{D}_s\mathbf{W}\dot{\mathbf{D}}_s \\ &= -\mathbf{D}_s\mathbf{D}_\omega\mathbf{W}\mathbf{D}_c - \mathbf{D}_c\mathbf{W}\mathbf{D}_s\mathbf{D}_\omega + \ldots \\ &\quad \mathbf{D}_c\mathbf{D}_\omega\mathbf{W}\mathbf{D}_s + \mathbf{D}_s\mathbf{W}\mathbf{D}_c\mathbf{D}_\omega \\ &= -\mathbf{D}_\omega(\mathbf{D}_s\mathbf{W}\mathbf{D}_c - \mathbf{D}_c\mathbf{W}\mathbf{D}_s) + \ldots \\ &\quad (\mathbf{D}_s\mathbf{W}\mathbf{D}_c - \mathbf{D}_c\mathbf{W}\mathbf{D}_s)\mathbf{D}_\omega \\ &= -\mathbf{D}_\omega\mathbf{C}_0 + \mathbf{C}_0\mathbf{D}_\omega.\end{aligned} \tag{27}$$

Substituting (20) and (27) in (26) yields

$$\mathbf{K} = \dot{\mathbf{M}} - 2\mathbf{C} = -\mathbf{D}_\omega\mathbf{C}_0 - \mathbf{C}_0\mathbf{D}_\omega. \tag{28}$$

Since $\mathbf{D}_\omega$ is diagonal and $\mathbf{C}_0^\top = -\mathbf{C}_0$ from Lemma 1, it follows that

$$\mathbf{K}^\top = (-\mathbf{D}_\omega\mathbf{C}_0 - \mathbf{C}_0\mathbf{D}_\omega)^\top \tag{29}$$
$$= \mathbf{C}_0\mathbf{D}_\omega + \mathbf{D}_\omega\mathbf{C}_0 \tag{30}$$
$$= -\mathbf{K} \tag{31}$$

Thus, the matrix defined by $\mathbf{K}$ is skew-symmetric. □

Remark 1 The dynamics can also be represented in relative coordinates by performing the substitutions $\mathbf{q} = \mathbf{\Phi}^{-1}\mathbf{r}$, $\dot{\mathbf{q}} = \mathbf{\Phi}^{-1}\dot{\mathbf{r}}$ and $\ddot{\mathbf{q}} = \mathbf{\Phi}^{-1}\ddot{\mathbf{r}}$.

3.1 Physical Parameters

The physical parameters used in this paper for benchmarking, chaos analysis, and experimental validation are summarized in Table 1. These correspond to the custom-built 10-link experimental platform described in Section 6; links 2–9 share the intermediate parameters, with link 1 carrying the mounting hardware and link 10 being the free tip.

4 Analytical Jacobian

The state vector is defined as $\mathbf{x} = \begin{bmatrix}\mathbf{q} & \dot{\mathbf{q}}\end{bmatrix}^\top \in \mathbb{R}^{2n}$. From (18), the state transition function $f(\cdot)$ can be written as

$$\dot{\mathbf{x}} = f(\mathbf{x}) = \begin{bmatrix}\dot{\mathbf{q}} \\ \ddot{\mathbf{q}}\end{bmatrix} \tag{32}$$

with

$$\ddot{\mathbf{q}} = \mathbf{M}(\mathbf{q})^{-1}\Big(\tau_{f,q}(\dot{\mathbf{q}}) - \mathbf{C}(\mathbf{q}, \dot{\mathbf{q}})\dot{\mathbf{q}} - \mathbf{g}(\mathbf{q})\Big). \tag{33}$$

Table 1: Dynamic and kinematic parameters of the n-link pendulum

Parameter	**Symbol**	**Link 1 (Base)**	**Link i (Inter.)**	**Link e (Tip)**
Mass (kg)	m_j	2.3181×10^{-2}	3.5146×10^{-3}	3.5671×10^{-3}
CoM Distance (m)	l_{cj}	2.5521×10^{-3}	2.8677×10^{-2}	2.9394×10^{-2}
Moment of Inertia (kg·m^2)	I_j	3.2877×10^{-6}	1.1693×10^{-6}	1.2597×10^{-6}
Total Link Length (m)	l_j	5.2520×10^{-2}	5.6720×10^{-2}	—
Viscous friction coefficient (Nms/rad)	b_j	1.8973×10^{-10}	1.7218×10^{-6}	1.7218×10^{-6}
Coulomb friction coefficient (Nm)	c_j	0.001×10^{0}	7.3479×10^{-6}	7.3479×10^{-6}

Note: Subscript $j \in \{1, i, e\}$ denotes the base, intermediate and tip links respectively

The analytical Jacobian $\mathbf{F}(\mathbf{x}) \in \mathbb{R}^{2n\times 2n}$ plays a central role in both the nonlinear dynamics analysis and model-based estimation of high-DOF pendulum chains. First, $\mathbf{F}(\mathbf{x})$ defines the variational dynamics $\delta\dot{\mathbf{x}} = \mathbf{F}(\mathbf{x})\delta\mathbf{x}$, which quantifies the evolution of infinitesimal perturbations along a trajectory. Second, it is required in the prediction step of the EKF, where it governs the first-order propagation of uncertainty and determines whether the linearization remains valid between measurement updates. In high-DOF chains, finite-difference Jacobians are both computationally expensive and numerically fragile. An exact closed-form expression improves the runtime while preserving the structural properties induced by the underlying dynamics.

The Jacobian has the block structure

$$\mathbf{F}(\mathbf{x}) = \begin{bmatrix} \mathbf{0}_{n\times n} & \mathbf{I}_n \\ \mathbf{F}_1(\mathbf{x}) & \mathbf{F}_2(\mathbf{x}) \end{bmatrix}. \tag{34}$$

where the matrices $\mathbf{F}_1,\ \mathbf{F}_2 \in \mathbb{R}^{n\times n}$ are defined as

$$\mathbf{F}_1(\mathbf{x}) = \frac{\partial \ddot{\mathbf{q}}}{\partial \mathbf{q}} \tag{35}$$

$$\mathbf{F}_2(\mathbf{x}) = \frac{\partial \ddot{\mathbf{q}}}{\partial \dot{\mathbf{q}}}. \tag{36}$$

Let $\mathbf{e}_k \in \mathbb{R}^n$ denote the k-th basis vector and define

$$\mathbf{E}_k = \mathbf{e}_k \mathbf{e}_k^\top,$$

which is a diagonal matrix with a single 1 at the index (k, k). Thus, the partial derivatives of the diagonal sine and cosine matrices with respect to the q_k'th absolute angle are defined as follows:

$$\frac{\partial \mathbf{D}_c}{\partial q_k} = -\mathbf{E}_k \mathbf{D}_s, \qquad \frac{\partial \mathbf{D}_s}{\partial q_k} = \mathbf{E}_k \mathbf{D}_c. \tag{37}$$

The structured matrices (22)–(23) satisfy the following identities, whose derivations are provided in Appendix A.

$$\frac{\partial \mathbf{M}_0}{\partial q_k} = \mathbf{C}_0 \mathbf{E}_k - \mathbf{E}_k \mathbf{C}_0, \tag{38}$$

$$\frac{\partial \mathbf{C}_0}{\partial q_k} = -\mathbf{M}_0 \mathbf{E}_k + \mathbf{E}_k \mathbf{M}_0. \tag{39}$$

Since $\mathbf{M}(\mathbf{q}) = \mathbf{M}_0(\mathbf{q}) + \mathbf{D}_I$, the derivative of the mass matrix with respect to q_k can be written as

$$\frac{\partial \mathbf{M}}{\partial q_k} = \mathbf{C}_0 \mathbf{E}_k - \mathbf{E}_k \mathbf{C}_0. \tag{40}$$

The dynamics are written in a more compact form as

$$\mathbf{M}(\mathbf{q})\ddot{\mathbf{q}} = \mathbf{n}(\mathbf{q}, \dot{\mathbf{q}}) \tag{41}$$

with $\mathbf{n}$ defined as

$$\mathbf{n}(\mathbf{q}, \dot{\mathbf{q}}) = \tau_{f,q}(\dot{\mathbf{q}}) - \mathbf{C}(\mathbf{q}, \dot{\mathbf{q}})\dot{\mathbf{q}} - \mathbf{g}(\mathbf{q}).$$

Implicitly differentiating (41) with respect to q_k and isolating $\frac{\partial \ddot{\mathbf{q}}}{\partial q_k}$ yields

$$\frac{\partial \ddot{\mathbf{q}}}{\partial q_k} = \mathbf{M}^{-1}\left(\frac{\partial \mathbf{n}}{\partial q_k} - \frac{\partial \mathbf{M}}{\partial q_k}\ddot{\mathbf{q}}\right). \tag{42}$$

Since the friction torque $\tau_{f,q}$ does not explicitly depend on $\mathbf{q}$, the partial derivative of $\mathbf{n}$ can be written as

$$\frac{\partial \mathbf{n}}{\partial q_k} = -\frac{\partial \mathbf{C}\dot{\mathbf{q}}}{\partial q_k} - \frac{\partial \mathbf{g}}{\partial q_k}.$$

Using (20) the partial derivative is rewritten explicitly as

$$\frac{\partial (\mathbf{C}\dot{\mathbf{q}})}{\partial q_k} = \frac{\partial \mathbf{C}_0}{\partial q_k}\mathbf{D}_\omega \dot{\mathbf{q}}$$

$$= \big(-\mathbf{M}_0\mathbf{E}_k + \mathbf{E}_k\mathbf{M}_0 \big)\mathbf{D}_\omega\dot{\mathbf{q}}. \tag{43}$$

The partial derivative of the gravity term is

$$\frac{\partial \mathbf{g}}{\partial q_k} = g\mathbf{E}_k\mathbf{D}_c\mathbf{\Lambda}^\top\mathbf{D}_m\mathbf{1} \tag{44}$$

Finally, the sub matrix $\mathbf{F}_1$ can be formed as

$$\mathbf{F}_1(\mathbf{x}) = \begin{bmatrix} \dfrac{\partial \ddot{\mathbf{q}}}{\partial q_1} & \cdots & \dfrac{\partial \ddot{\mathbf{q}}}{\partial q_n} \end{bmatrix} \tag{45}$$

by evaluating Eq. (42) n times using Eq. (40).

The sub matrix $\mathbf{F}_2$ is defined as

$$\mathbf{F}_2 = \mathbf{M}^{-1}\frac{\partial \mathbf{n}}{\partial \dot{\mathbf{q}}} = \mathbf{M}^{-1}\left(\frac{\partial \tau_{f,q}}{\partial \dot{\mathbf{q}}} - \frac{\partial(\mathbf{C}\dot{\mathbf{q}})}{\partial \dot{\mathbf{q}}}\right). \tag{46}$$

The partial derivative of the absolute friction torque defined in (9) is written as a chain rule

$$\frac{\partial \tau_{f,q}}{\partial \dot{\mathbf{q}}} = \frac{\partial \tau_{f,q}}{\partial \dot{\mathbf{r}}}\frac{\partial \dot{\mathbf{r}}}{\partial \dot{\mathbf{q}}} = \mathbf{\Phi}^\top\frac{\partial \tau_{f,r}}{\partial \dot{\mathbf{r}}}\mathbf{\Phi}$$

Using the friction model defined in (10) we can write the partial derivative of the friction torque in absolute coordinates explicitly as

$$\frac{\partial \tau_{f,q}}{\partial \dot{\mathbf{q}}} = \mathbf{\Phi}^\top\left[-\mathbf{D}_B - \frac{\mathbf{D}_C}{\varepsilon}\operatorname{sech}^2(\mathbf{\Phi}\dot{\mathbf{q}}/\varepsilon)\right]\mathbf{\Phi} \tag{47}$$

Using $\mathbf{C}\dot{\mathbf{q}} = \mathbf{C}_0\mathbf{D}_\omega\dot{\mathbf{q}}$, we obtain the closed-form derivative

$$\frac{\partial(\mathbf{C}\dot{\mathbf{q}})}{\partial \dot{\mathbf{q}}} = \mathbf{C}_0\,\mathrm{diag}(2\dot{\mathbf{q}}), \tag{48}$$

Thus, the continuous-time Jacobian matrix defined in (34) can be formed by evaluating the submatrices.

4.1 Verification and Computational Performance

Before applying the closed-form dynamics and analytical Jacobian to the chaos analysis and state estimation, we verified their numerical correctness and quantified their computational cost relative to the standard alternatives. Two properties were examined: energy conservation along the simulated trajectories and agreement between the analytical Jacobian and high-order central-difference numerical Jacobian. All benchmarks were executed in MATLAB on a PC with an i7-14700K processor and 64 GB of RAM.

4.1.1 Numerical accuracy

For a frictionless n-link pendulum, the total mechanical energy $E(t) = T(t) + U(t)$ must be conserved. Therefore, this quantity serves as an integrity check on the dynamics implementation. The trajectories were integrated using a classical fourth-order Runge-Kutta scheme with a fixed step $\Delta t = 10^{-3}$ s over a horizon of $T = 50$ s. For each link count $n \in [5,\ 10,\ 15]$, 40 random initial conditions are drawn with $\mathbf{q}_0 \sim \mathcal{U}[-\pi/4,\ \pi/4]^n$ rad and $\dot{\mathbf{q}}_0 \sim \mathcal{U}[-2,\ 2]^n$ rad/s. Across all tested link counts, the relative energy drift $|E(t) - E(0)|\ /\ |E(0)|$ remains bounded by 10^{-2} for the total integration time, as illustrated in Fig. 2a. Until $T = 0.1$ s, the relative drift is consistent with the floating-point precision of the integrator and confirms that the closed-form dynamics preserve the Hamiltonian structure of the system.

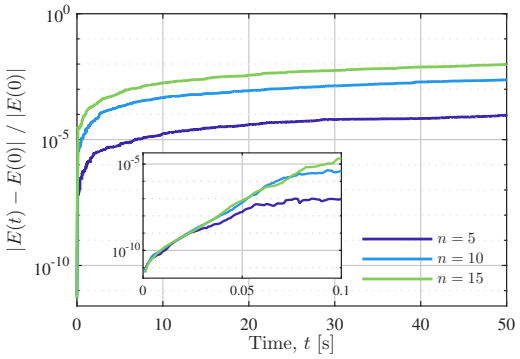
The analytical Jacobian $\mathbf{F}(\mathbf{x})$ is further validated against a central-difference numerical Jacobian

$$F_{ij}^{\mathrm{FD}}(x) = \frac{f_i(\mathbf{x} + h\mathbf{e}_j) - f_i(\mathbf{x} - h\mathbf{e}_j)}{2h}, \tag{49}$$

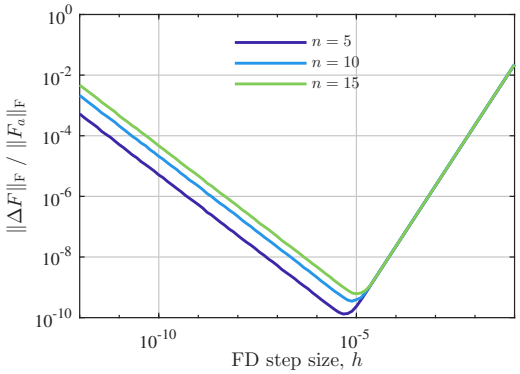
evaluated over 1000 random states per n. The angle and angular velocities were initialized as $q \in [-\pi/4, \pi/4]$ and $\dot{q} \in [-2, 2]$ rad/s respectively. The results are shown in Fig. 2b. At the optimal step size of $h \approx 10^{-5}$, the relative Frobenius-norm error $\left\|\mathbf{F} - \mathbf{F}^{\mathrm{FD}}\right\|_F / \left\|\mathbf{F}\right\|_F$ for $n = 15$ was $6.108 \cdot 10^{-10}$, consistent with the expected balance between truncation and round-off error in central differences.

4.1.2 Timing performance

To assess the practical computational cost of the proposed formulation, we benchmarked the per-call evaluation time of the forward dynamics $f(\mathbf{x})$ and analytical Jacobian $\mathbf{F}(\mathbf{x})$ as a function of the link count n. The proposed closed-form dynamics are compared with the iterative formulation in [2]. The forward dynamics were solved using a 4th order fixed-step solver with a step size of 0.001 s for a total of 5 s. The initial angles were set as $\pi/8$ with alternating signs, and the angular velocities



(a)



(b)

Fig. 2: Numerical accuracy of the closed-form dynamics for $n \in \{5, 10, 15\}$. **(a)** Relative energy drift over 50 s; inset zooms into the first 0.1 s. **(b)** Relative Frobenius error between the analytical and central-difference Jacobians versus step size h

were set to 0. This was done to ensure identical conditions as [2]. The computational performance was computed for 50 trials per n, where n was evaluated from 1 to 40. The timing for each trial was then averaged over each n to obtain a mean timing value. The analytical Jacobian is compared with a central-difference numerical Jacobian built from the same closed-form $f(\mathbf{x})$ as in (49). The Jacobian is evaluated directly by assigning 50 random initial conditions per n and evaluating each condition 100 times. The timing was then averaged to obtain the mean time to run a single loop of the Jacobian algorithm.

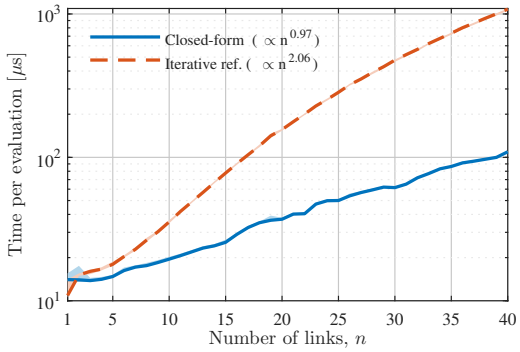
Fig. 3a shows the resulting median per-evaluation time of the forward dynamics, with shaded interquartile bands across the 50 trials. A linear least-squares fit on log$t$ versus log n, restricted to $n \geq 4$ to avoid the small-n regime in which constant-overhead costs dominate, yields an empirical scaling of $t \propto n^{0.97}$ for the closed-form formulation and $t \propto n^{2.06}$ for the iterative reference. Although the asymptotic complexity of the closed-form dynamics is bounded by the $O(n^3)$ cost of the inertia-matrix solve $M^{-1}n(q, \dot{q})$, the empirical scaling within the operating range $n \in [1, 40]$ is dominated by the cache-resident $O(n^2)$ matrix construction.

Fig. 3b reports the corresponding benchmark for the Jacobian. The analytical Jacobian exhibits empirical scaling of $t \propto n^{0.62}$, whereas the central-difference numerical Jacobian scales as $t \propto n^{1.89}$ owing to its $2n$ additional dynamics evaluations per Jacobian call. The benchmark establishes both the asymptotic and practical advantages of the closed-form derivations and motivates their use throughout the remainder of the paper.

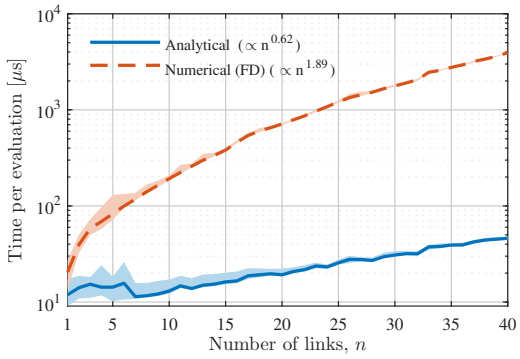
The scaling reported here characterizes the closed-form formulation against the specific iterative reference of [2] within $n \in [1, 40]$; recursive multibody algorithms such as the articulated-body algorithm achieve linear-in-n floating-point counts and would scale more favorably at very large n. The value of the closed-form expression in this paper lies less in absolute speed than in the properties it provides: an analytical Jacobian in the same structured operands, the closed-form skew-symmetry of $\dot{\mathbf{M}} - 2\mathbf{C}$ established in Lemma 2, and a constant coupling matrix $\mathbf{W}$ computed once. None of these is automatic in a recursive pipeline, and together they enable the Benettin–QR variational integration of Section 5.4 and the EKF prediction step of Section 7.2 without recourse to finite-difference Jacobians.

5 Chaos analysis

The closed-form dynamics and analytical Jacobian derived in Sections 3 and 4 enable a systematic chaos analysis of the conservative n-link pendulum across a range of link counts. Two complementary tools were employed. Recurrence plot (RP) analysis provides a topological view of the trajectory's return structure in phase space, with Recurrence Quantification Analysis (RQA) extracting scalar measures of determinism and predictability from the binary recurrence matrix. The full Lyapunov



(a)



(b)

Fig. 3: Per-evaluation timing versus link count n. **(a)** Forward dynamics. **(b)** Jacobian. Bands denote interquartile range across 50 trials per n

spectrum is computed via the Benettin–QR algorithm, with the analytical Jacobian propagating the variational dynamics exactly in the tangent space. Both analyses are run on the same trajectories so that the recurrence statistics and Lyapunov exponents can be cross-checked at every n. The physical parameters listed in Table 1 are used in this paper. All chaos-related analyses were performed in `Julia` using the ChaosTools toolbox for convenience [48].

5.1 Simulation Setup

For each link count n, the equations of motion were integrated in Julia using the `Vern9` solver with tight tolerances (RelTol $= 10^{-10}$, AbsTol $= 10^{-12}$) over a horizon of $T = 10\,\mathrm{s}$ with a fixed output step of $\Delta t = 0.005\,\mathrm{s}$, yielding $N = 2001$ samples per trajectory. The same trajectories are used for both the recurrence analysis in Sections 5.2–5.3 and the Lyapunov spectrum in Section 5.4. All post-processing and visualizations were performed using MATLAB.

To ensure a fair energy-normalized comparison across different n, the initial state is constructed at a fixed fraction $U_{\mathrm{frac}} \in [0, 1]$ of the maximum potential energy. The maximum potential energy is attained when every link points upward ($\cos q_i = -1$ for all i), giving

$$U_{\max} = 2g\,\mathbf{1}^\top \mathbf{D}_m \mathbf{\Lambda}\,\mathbf{1}. \tag{50}$$

The initial state vector is set to alternating-sign angular displacements with zero initial velocities,

$$\mathbf{x}(0) = \big[q_0,\, -q_0,\, q_0,\, -q_0,\, \ldots,\, 0,\, 0,\, \ldots\big]^\top,$$

with the common amplitude derived by matching the initial configuration energy to the desired fraction $U(0) = U_{\mathrm{frac}} U_{\max}$

$$q_0 = \arccos\big(1 - 2U_{\mathrm{frac}}\big). \tag{51}$$

To verify that this choice of q_0 satisfies the energy constraint, we substitute the initial configuration $\mathbf{c}(\mathbf{q}) = \cos(q_0)\mathbf{1}$ back into the potential energy formulation in Equation (13):

$$\begin{aligned} U(0) &= g\,\mathbf{1}^\top \mathbf{D}_m \mathbf{\Lambda}\big(\mathbf{1} - \cos(q_0)\mathbf{1}\big) \\ &= \big(1 - \cos(q_0)\big) g\,\mathbf{1}^\top \mathbf{D}_m \mathbf{\Lambda}\,\mathbf{1}. \end{aligned}$$

Substituting the relation $\cos(q_0) = 1 - 2U_{\mathrm{frac}}$ implied by Equation (51) yields

$$\begin{aligned} U(0) &= \big(1 - (1 - 2U_{\mathrm{frac}})\big) g\,\mathbf{1}^\top \mathbf{D}_m \mathbf{\Lambda}\,\mathbf{1} \\ &= 2U_{\mathrm{frac}} \cdot g\,\mathbf{1}^\top \mathbf{D}_m \mathbf{\Lambda}\,\mathbf{1}. \end{aligned}$$

Recalling the definition of $U_{\max}$ from Equation (50), $U(0) = U_{\mathrm{frac}} U_{\max}$ as required.

We use $U_{\mathrm{frac}} = 0.25$ throughout all analyses unless otherwise specified.

5.2 Recurrence Plots

A recurrence plot [36] visualizes the binary recurrence matrix

$$R_{i,j}(\varepsilon) = \Theta\big(\varepsilon - \|\tilde{\mathbf{x}}_i - \tilde{\mathbf{x}}_j\|_2\big), \quad i, j = 1, \ldots, N, \tag{52}$$

where $\Theta(\cdot)$ is the Heaviside function and $\tilde{\mathbf{x}}_i$ denotes the i-th sample of an embedded phase-space trajectory.

Phase-space embedding and normalization. The configuration of an n-link pendulum lives on the n-torus $\mathbb{T}^n$, and the raw angles $q_i \in \mathbb{R}$ contain 2π-wrap discontinuities that produce spurious large pairwise distances at the branch cuts. We therefore embed each sample as

$$\tilde{\mathbf{x}}_i = \left[\sin \mathbf{q}^\top,\ \cos \mathbf{q}^\top,\ z(\dot{\mathbf{q}})^\top\right]^\top \in \mathbb{R}^{3n}, \qquad (53)$$

where $z(\cdot)$ denotes column-wise z-score normalization (zero mean, unit variance) of the angular velocity time series across the N samples. The pair $(\sin q_i, \cos q_i)$ embeds $\mathbb{T}^n$ smoothly into $\mathbb{R}^{2n}$ such that two states differing by an integer multiple of 2π in any joint are correctly identified, and is bounded in $[-1, 1]$. Normalizing $\dot{\mathbf{q}}$ in turn brings the velocity channels onto a comparable scale; without this step, the velocity spread, which grows with n at a fixed energy, would dominate the Euclidean distance in (52).

Threshold selection. A common approach is to set ε as a fixed fraction of the maximum phase space diameter. Because the maximum pairwise distance is sensitive to outliers and scales with the dimension, such a rule yields incomparable recurrence densities across different n. We adopt a fixed recurrence-rate strategy [36]: the threshold ε is chosen such that the target recurrence rate $\mathrm{RR} = 10\%$ is achieved. All distances $d_{ij} = \|\tilde{\mathbf{x}}_i - \tilde{\mathbf{x}}_j\|_2$ satisfying $|i-j| > w$ are collected, and ε is set equal to their 10^{th} percentile. Throughout this work, we use a Theiler window of $w = 10$ samples (0.05 s), chosen to exclude temporally correlated neighbors from both the threshold calibration and the recurrence statistics of Section 5.3. This procedure guarantees equal recurrence density in every plot, so that cross-n comparisons of the recurrence structure are not confounded by density differences.

Qualitative observations. Fig. 4 shows the recurrence plots for $n = 1$ to $n = 12$, displayed over the first 10 s of each trajectory. The $n = 1$ panel is dominated by long unbroken diagonals parallel to the line of identity (LOI). The simple pendulum at this energy oscillates regularly, and the trajectory revisits the same neighborhood at nearly constant intervals. For $n = 2$, the long diagonals persist but are interspersed with fragmented segments and isolated recurrence points, indicating the onset of chaotic mixing, while a substantial deterministic structure remains.

The visual characteristics changed abruptly at $n = 3$. The long diagonals break apart into short segments, and the salt-and-pepper texture characteristic of strongly chaotic dynamics begins to fill the plots. The $n = 4$ and $n = 5$ panels show similar textures with occasional short diagonal clusters.

For $n \geq 6$, the recurrence structure becomes visually indistinguishable across the link counts: short diagonals coexist with isolated points, and no extended coherent features survive. Across the full range $n = 1, \ldots, 12$, the visual transition from ordered to chaotic topology is monotonic, with the most pronounced change occurring between $n = 2$ and $n = 3$ and no order–chaos–order reversals at the energy level and initial conditions considered here.

5.3 Recurrence Quantification Analysis

To move beyond visual inspection, the recurrence structure is quantified using standard RQA measures [36], computed over the full 10s trajectory using the `ChaosTools.jl` toolbox. A minimum diagonal line length of $\ell_{\min} = 15$ samples (0.075 s) was used to filter out short correlations arising from the finite output step rather than from genuine dynamical recurrence, and the same Theiler window of $w = 10$ samples was applied throughout.

The following measures are summarized numerically in Table 2.

- **Recurrence rate (RR):** the fraction of recurrent pairs in the binary matrix (52), included as a consistency check confirming that the fixed-RR threshold calibration of Section 5.2 indeed yields $\mathrm{RR} \approx 10\%$ for every n.
- **Determinism (DET):** the fraction of recurrence points belonging to diagonal lines of length $\geq \ell_{\min}$. A high DET indicates predictable and deterministic dynamics, whereas a

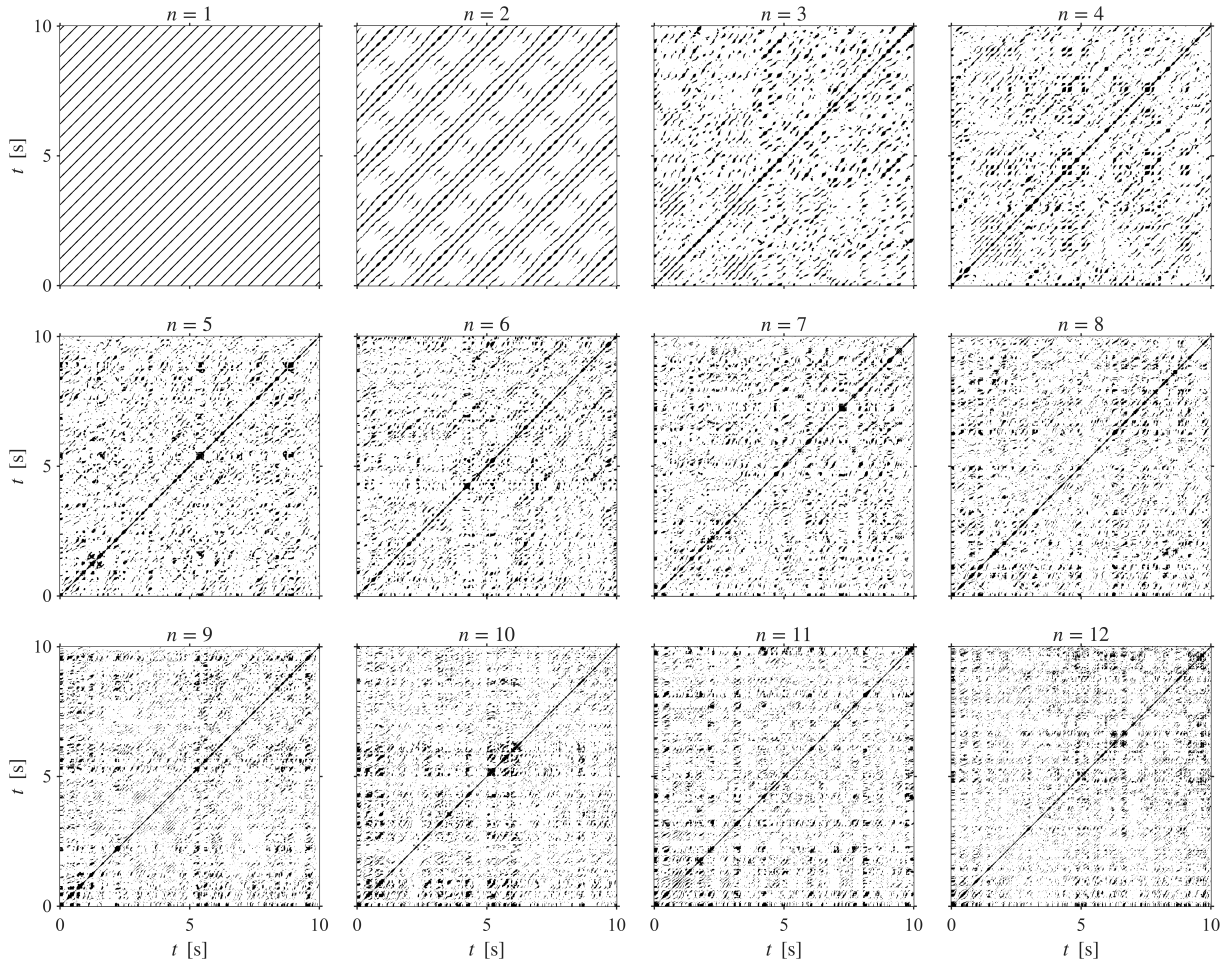


Fig. 4: Recurrence plots of the n-link pendulum for $n = 1, \ldots, 12$ over the first 10 s of each trajectory, in the embedding of Eq. (53). Threshold ε calibrated per n to RR = 10%; Theiler window $w = 10$ samples

low DET indicates chaotic or stochastic behavior [36].

- **Mean diagonal length (L):** the average length of diagonal lines, providing a direct measure of the typical prediction horizon over which neighbouring trajectories remain close.
- **Longest diagonal line ($L_{\max}$):** the length of the longest diagonal line in the recurrence matrix. $L_{\max}$ is inversely related to the dominant instability rate, with a shorter $L_{\max}$ implying a faster divergence of nearby trajectories.

Results.

Table 2 reports the RQA statistics together with the relative energy drift $|\Delta E|/|E_0|$ over the full integration window, which is included as a numerical integrity check. The recurrence rate stays within 0.6% of the 10% target across all link counts, confirming the threshold calibration, and the energy drift remains below $8{\times}10^{-11}$ throughout, consistent with the prescribed `Vern9` tolerances and confirming that the Hamiltonian structure is preserved across all simulated trajectories.

The diagonal line measures decrease with n in a manner that identifies two distinct regimes. DET falls monotonically from 97.1% at $n = 1$ to 10.1% at $n = 12$, quantifying the progressive disappearance of the extended deterministic structure as the chain grows. The longest diagonal $L_{\max}$ exhibits the sharpest transition: it remains close to the trajectory length ($\sim$2001 samples) for $n \leq 2$, then drops by nearly two orders of magnitude between $n = 2$ and $n = 3$ (from 1579 to 124 samples), after which it decays to the range

Table 2: RQA metrics and relative energy drift for the n-link pendulum over a 10 s trajectory at $U_{\text{frac}} = 0.25$

n	RR	DET	L	$L_{\max}$	$\Delta E/\lvert E_0\rvert$
1	0.096	0.971	275.79	1901	7.88×10^{-11}
2	0.094	0.845	36.18	1579	6.85×10^{-11}
3	0.093	0.589	24.56	124	4.09×10^{-11}
4	0.093	0.515	23.15	77	2.40×10^{-11}
5	0.094	0.313	21.11	70	1.74×10^{-11}
6	0.094	0.284	20.51	79	2.57×10^{-11}
7	0.094	0.272	20.40	56	3.00×10^{-11}
8	0.094	0.259	20.68	52	3.39×10^{-11}
9	0.094	0.191	20.28	49	4.11×10^{-11}
10	0.094	0.203	21.96	57	4.76×10^{-11}
11	0.095	0.205	21.14	57	3.14×10^{-11}
12	0.095	0.101	18.45	45	4.24×10^{-11}

45–77 samples for $n \geq 4$. This step change is consistent with the qualitative shift in the recurrence topology observed in Fig. 4, where the long diagonals characteristic of (quasi-)periodic motion at $n = 1, 2$ break apart into fragmented short segments associated with strongly chaotic trajectories from $n = 3$ onward.

The mean diagonal length L exhibited a complementary two-stage behavior. It contracts sharply from 276 (1.38 s) samples at $n = 1$ to 36 samples (0.18 s) at $n = 2$, then plateaus around 18–24 samples for all $n \geq 3$. The plateau indicates that once the chain has entered the high-DOF chaotic regime, the typical span of coherent recurrence is set by the local dynamics on a sub-second timescale and becomes essentially insensitive to the dimension. The Lyapunov spectrum analysis in Section 5.4 provides an independent quantitative confirmation of these trends.

5.4 Lyapunov exponents

The full spectrum of $2n$ Lyapunov characteristic exponents (LCEs) is computed using the classical Benettin–QR algorithm [26, 27]. The key advantage over time-series–based estimators [29, 30] is that the analytical Jacobian $\mathbf{F}(\mathbf{x})$ derived in Section 4 is available, so the variational (tangent-space) dynamics

$$\delta\dot{\mathbf{x}} = \mathbf{F}(\mathbf{x}(t))\,\delta\mathbf{x} \tag{54}$$

can be integrated exactly alongside the reference trajectory without finite-difference approximations, eliminating both a source of truncation error and the $\mathcal{O}(n)$ overhead per Jacobian evaluation that finite differences would incur at every QR step.

An orthonormal frame $\mathbf{Q}(t) \in \mathbb{R}^{2n\times 2n}$ is initialized as $\mathbf{Q}(0) = I_{2n}$ and propagated forward in time by integrating the matrix ODE $\dot{\mathbf{Q}} = \mathbf{F}(\mathbf{x}(t))\mathbf{Q}$ with the same `Vern9` solver and tolerances used for the reference trajectory for $T = 10\,\text{s}$ with a fixed output step of $\Delta t = 0.005\,\text{s}$. Every 10 output steps (0.05 s), a QR decomposition $\mathbf{Q} = \hat{\mathbf{Q}}\hat{\mathbf{R}}$ is performed: the orthonormal factor $\hat{\mathbf{Q}}$ replaces $\mathbf{Q}$ to prevent the columns from collapsing onto the most-unstable direction, and the diagonal of the upper-triangular factor $\hat{\mathbf{R}}$ is accumulated in

$$\lambda_i = \frac{1}{T}\sum_{j=1}^{N_{\text{ren}}} \ln\bigl|R_{ii}^{(j)}\bigr|, \qquad i = 1, \ldots, 2n, \tag{55}$$

where $T = (N-1)\Delta t$ is the total integration time, and N_{ren} is the number of re-orthonormalizations. The exponents are sorted in descending order, so $\lambda_1 \equiv \lambda_{\max}$ is the largest Lyapunov exponent (LLE).

For a Hamiltonian (conservative) system, the Lyapunov spectrum must satisfy two structural properties: the exponents occur in conjugate pairs $(\lambda_i, -\lambda_i)$, and their sum vanishes, $\sum_{i=1}^{2n}\lambda_i = 0$, reflecting volume preservation in the phase space (Liouville's theorem). Across all simulated trajectories, the residual spectrum sum satisfies $\bigl|\sum_i \lambda_i\bigr| < 0.044\,\text{s}^{-1}$, and the pairing symmetry $\lambda_i \approx -\lambda_{2n+1-i}$ holds within numerical precision, providing an independent confirmation of both the analytical Jacobian derivation and variational integration.

Largest Lyapunov exponent and onset of hyperchaos.

Fig. 5 shows the two leading Lyapunov exponents $\lambda_{\max}$ and λ_2 as functions of n. For the single-link pendulum ($n = 1$), $\lambda_{\max} \approx 0$, which is consistent with the integrable nature of the simple pendulum. At $n = 2$, $\lambda_{\max}$ becomes weakly positive ($\approx 0.157\,\text{s}^{-1}$) while λ_2 remains indistinguishable from zero, indicating chaos with a single unstable direction in the tangent space. The qualitative

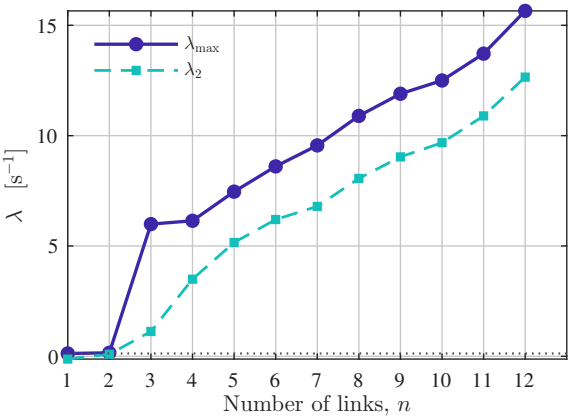


Fig. 5: Two leading Lyapunov exponents $\lambda_{\max}$ (solid) and λ_2 (dashed) of the n-link pendulum versus link count n at $U_{\text{frac}} = 0.25$

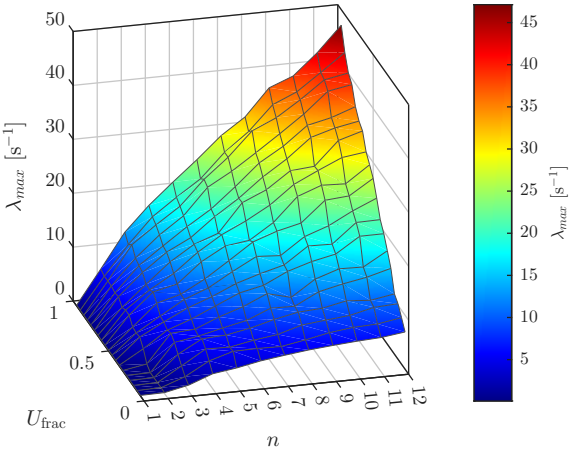


Fig. 6: Largest Lyapunov exponent $\lambda_{\max}$ as a function of link count n and initial energy fraction U_{frac}

behavior changes sharply at $n = 3$; both $\lambda_{\max}$ and λ_2 jump by more than an order of magnitude, signalling the onset of hyperchaos, in which the trajectory has at least two independent directions of exponential divergence. For $n \geq 3$ both exponents continue to grow monotonically, $\lambda_{\max}$ reaching $15.654\,\text{s}^{-1}$ at $n = 12$. This growth reflects the expanding dimensionality of the phase space and the increasingly complex interlink coupling.

Because the LLE is also energy-dependent, an additional analysis using different U_{frac} values for each n was performed and is shown in Fig. 6. A similar characteristic is observed when n changes from 2 to 3, where a steep increase in the LLE indicates the transition to hyperchaos, even across different energy levels, which further strengthens the claim.

Full Lyapunov spectrum.

Fig. 7 displays the full sorted spectrum $\{\lambda_i\}_{i=1}^{2n}$ at representative link counts $n \in \{2, 4, 8, 12\}$. At $n = 2$, the spectrum consists of a single weakly positive exponent, its conjugate negative partner, and a near-zero pair, consistent with the marginal-chaos regime identified above. At $n = 4$, multiple strictly positive exponents are present, and the envelope of the spectrum spans approximately $[-5, 5]\,\text{s}^{-1}$. By $n = 12$, approximately half of the $2n = 24$ exponents are positive, and the envelope reaches $\sim 15\,\text{s}^{-1}$, indicating strongly hyperchaotic dynamics in the system. The conjugate-pair symmetry $\lambda_i \approx -\lambda_{2n+1-i}$ is visible in every spectrum, and

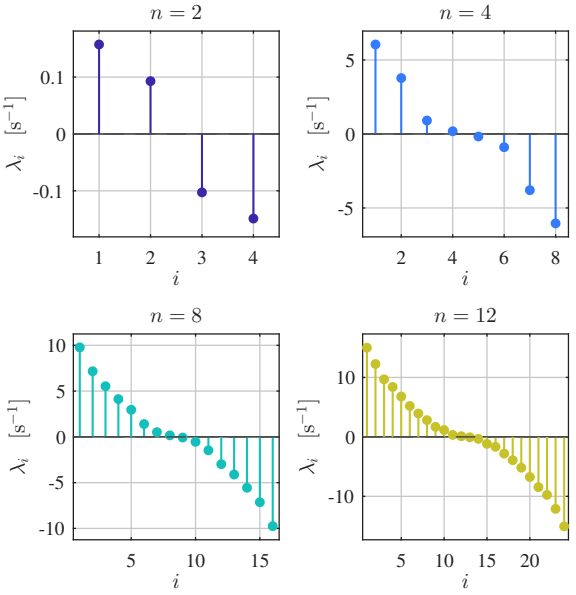


Fig. 7: Full Lyapunov spectrum $\{\lambda_i\}_{i=1}^{2n}$ at $n \in \{2, 4, 8, 12\}$, sorted in descending order

the broadening envelope reflects both a stronger maximal instability and a stronger maximal contraction in the tangent space.

Cross-validation with RQA.

The Lyapunov and recurrence analyses provide consistent and complementary characterizations of the loss of predictability with n. The monotonic increase of $\lambda_{\max}$ with n mirrors the monotonic

decrease of DET in Table 2, and the simultaneous lift-off of λ_2 from zero between $n = 2$ and $n = 3$ coincides with the order-of-magnitude collapse of $L_{\max}$ over the same interval, identifying this as the principal transition to the hyperchaotic regime. Beyond $n \geq 6$, both $\lambda_{\max}$ and λ_2 continue to grow, while L has already saturated at the plateau value of Section 5.3. This is the expected behavior: the Lyapunov exponents measure the exponential rates of divergence in the tangent space, whereas L measures the typical *duration* of coherent recurrence in the embedded trajectory.

6 Experimental setup and data

The efficient closed-form dynamic equations derived in the previous sections facilitate the experimental analysis of the n-link pendulum. The physical parameters used in the experimental setup are listed in Table 1. These parameters were obtained through CAD analysis and the authors' previous work in [47].

6.1 Hardware and sensing

To validate the proposed algorithm, we utilized the 10-link experimental setup developed by the authors [47]. For this study, the sensing apparatus was upgraded to capture the high-frequency dynamics more accurately. Instead of the previously used 120 Hz camera, marker positions were tracked using a Qualisys Miqus M3 motion capture (MoCap) camera operating at 600 Hz, with passive infrared markers at each joint to improve the tracking reliability. Additionally, the proposed algorithms were implemented on a dSPACE MicroAutoBox II to validate the performance of the estimator in real time. The experimental setup is shown in Fig. 8.

The MoCap camera reads the marker positions and sends them to the PC, which routes them to the real-time hardware on which the state estimation algorithms run.

6.2 Experimental procedure

The experimental procedure involved manually stabilizing the pendulum in an arbitrary initial configuration, initiating data acquisition of the 11 passive infrared markers, and then releasing the system to undergo an unforced motion. Once

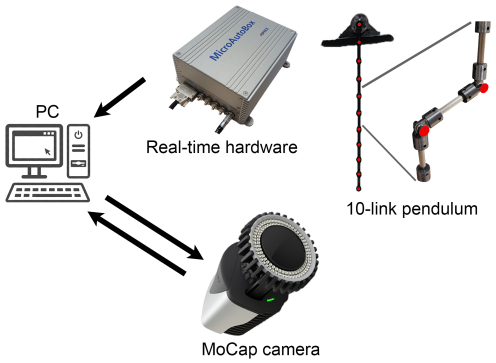


Fig. 8: Experimental setup: 10-link pendulum, Qualisys Miqus M3 motion-capture camera, and dSPACE MicroAutoBox II real-time hardware

the pendulum motion was naturally damped, the recording was terminated, and the dataset was saved for evaluation. Each trial contained the x and y positions of each marker in the system from the base to the tip. Because the base marker is stationary, its x and y positions are used as the origin of the measurements. The subsequent 10 markers are used directly and are stacked in the vectors $\mathbf{x}_m,\ \mathbf{y}_m \in \mathbb{R}^{10}$.

6.3 Data processing and availability

To facilitate reproducibility, all raw datasets generated in this paper are publicly accessible via [49]. The experimental data collection encompassed three distinct initial conditions designed to capture diverse dynamic behaviors: (i) a stationary calibration state, (ii) unforced motion initiated by deflecting only the first joint, and (iii) unforced motion following an arbitrary displacement of the distal link (joint 10). As summarized in Table 3, the recorded trials across these conditions varied systematically in terms of their total duration, sampling frequency, and number of independent executions.

The dataset is organized in folders, first by the type of initial condition, followed by the sampling rate, which contains each separate trial. For example, to access the 12th trial of the 20 s long 500 Hz experiment, one has to navigate to the folder `long -> 500 Hz -> measurement0012`. A helper loader function in MATLAB is provided as `loadNlinkExpData.m` for convenience. From this point in the paper, experiments will be referenced

Table 3: Experimental dataset configurations: initial condition, recording duration, sampling rate, and number of trials

Initial Condition	Duration (s)	Sampling Rate (Hz)	No. of Trials
Calibration (`calib`)	5	600	1
		300	1
Joint 1 Release (`base`)	20	600	10
Tip Arbitrary Release (`short, long`)	5	600	20
		500	20
		300	20
	20	600	30
		500	20

in shorthand notation as for example `(long, 500, 12)`.

The marker data were calibrated by setting the base marker as the origin of the system. Additionally, the units were converted from pixels to meters using a fixed conversion ratio $k = 9.38 \cdot 10^{-4}$.

7 Real-time state estimation

The motion capture system measures Cartesian marker positions, not the generalized coordinates $\mathbf{q}$ and $\dot{\mathbf{q}}$ required for state-based analyses. Therefore, we reconstruct the full state $\mathbf{x}$ from the Cartesian measurements using an Extended Kalman Filter (EKF). The analytical measurement Jacobian derived below, together with the dynamics Jacobian in Eq. (34), allows the EKF to be implemented without finite-difference approximations. The measurement vector is

$$\mathbf{z} = \begin{bmatrix} \mathbf{x_m} \\ \mathbf{y_m} \end{bmatrix}. \tag{56}$$

7.1 Process and measurement models

The n-link pendulum is a continuous-time nonlinear system observed through discrete-time measurements as follows:

$$\dot{\mathbf{x}}(t) = \mathbf{f}(\mathbf{x}(t)) + \mathbf{w}(t), \tag{57}$$
$$\mathbf{z}_k = \mathbf{h}(\mathbf{x}_k) + \mathbf{v}_k, \tag{58}$$

where $\mathbf{f}(\mathbf{x}(t))$ denotes the closed-form forward dynamics introduced in Section 3, and $\mathbf{h} : \mathbb{R}^{2n} \to \mathbb{R}^{2n}$ is the nonlinear measurement function

$$\mathbf{h}(\mathbf{x}_k) = \begin{bmatrix} \mathbf{L}\,\mathbf{s}(\mathbf{q}) \\ -\mathbf{L}\,\mathbf{c}(\mathbf{q}) \end{bmatrix}, \tag{59}$$

with $\mathbf{L} \in \mathbb{R}^{n \times n}$ the lower-triangular link-length matrix

$$\mathbf{L} = \begin{bmatrix} l_1 & 0 & \cdots & 0 \\ l_1 & l_2 & \cdots & 0 \\ \vdots & \vdots & \ddots & \vdots \\ l_1 & l_2 & \cdots & l_n \end{bmatrix}. \tag{60}$$

which encodes the cumulative kinematic chain from the base to each joint, and The corresponding measurement Jacobian is

$$\mathbf{H}(\mathbf{x}) = \frac{\partial \mathbf{h}}{\partial \mathbf{x}} = \begin{bmatrix} \mathbf{L}\mathbf{D}_c & \mathbf{0}_{n\times n} \\ \mathbf{L}\mathbf{D}_s & \mathbf{0}_{n\times n} \end{bmatrix}. \tag{61}$$

The zero blocks reflect that $\mathbf{h}$ depends only on the positions $\mathbf{q}$, and the velocity states $\dot{\mathbf{q}}$ are observed only indirectly through the dynamics.

The process noise $\mathbf{w}(t)$ is modeled as a zero-mean continuous-time white noise with power spectral density specified in Section 7.3, and $\mathbf{v}_k$ is a zero-mean discrete-time Gaussian sequence with covariance $\mathbf{R}$.

7.2 Prediction and update

The EKF operates in alternating prediction and update phases. In the prediction step, the state estimate is propagated by a fourth-order Runge–Kutta integration of the nonlinear dynamics, whereas the error covariance is propagated via the

discretized state-transition Jacobian $\mathbf{F}_{k-1}$:

$$\hat{\mathbf{x}}_{k|k-1} = \hat{\mathbf{x}}_{k-1|k-1} + \int_{t_{k-1}}^{t_k} \mathbf{f}(\hat{\mathbf{x}}(\tau))\, d\tau, \tag{62}$$

$$\mathbf{P}_{k|k-1} = \mathbf{F}_{k-1}\, \mathbf{P}_{k-1|k-1}\, \mathbf{F}_{k-1}^T + \mathbf{Q}_d, \tag{63}$$

where

$$\mathbf{F}_{k-1} \approx \mathbf{I} + \Delta t \left.\frac{\partial \mathbf{f}}{\partial \mathbf{x}}\right|_{\hat{\mathbf{x}}_{k-1|k-1}}, \tag{64}$$

Δt is the sampling period, and $\mathbf{Q}_d$ is the discrete-time process noise covariance defined in Section 7.3. Although the state is propagated to fourth-order accuracy, a first-order Euler approximation of $\mathbf{F}_{k-1}$ is retained for the covariance propagation.

When a new measurement is available, the update step corrects the prediction using the Kalman gain $\mathbf{K}_k$:

$$\mathbf{K}_k = \mathbf{P}_{k|k-1}\, \mathbf{H}_k^T \left(\mathbf{H}_k\, \mathbf{P}_{k|k-1}\, \mathbf{H}_k^T + \mathbf{R}\right)^{-1}, \tag{65}$$

$$\hat{\mathbf{x}}_{k|k} = \hat{\mathbf{x}}_{k|k-1} + \mathbf{K}_k \left(\mathbf{z}_k - \mathbf{h}(\hat{\mathbf{x}}_{k|k-1})\right), \tag{66}$$

$$\mathbf{P}_{k|k} = (\mathbf{I} - \mathbf{K}_k \mathbf{H}_k)\, \mathbf{P}_{k|k-1}, \tag{67}$$

where $\mathbf{H}_k = \mathbf{H}(\hat{\mathbf{x}}_{k|k-1})$ is the analytical measurement Jacobian evaluated at the predicted state.

The filter is implemented in a multi-rate configuration: the prediction runs at a fixed rate f_p, whereas updates occur asynchronously at the measurement rate $f_m \leq f_p$.

7.3 Filter tuning

Process noise covariance.

The discrete-time process noise covariance $\mathbf{Q}_d \in \mathbb{R}^{2n\times 2n}$ is derived from a continuous-time white-noise acceleration model, in which the unmodeled accelerations entering each joint are treated as independent white-noise processes. Integrating the resulting continuous-time covariance over one sampling interval yields

$$\mathbf{Q}_d = \begin{bmatrix} \mathbf{\Phi}_s\, T_s^3/3 & \mathbf{\Phi}_s\, T_s^2/2 \\ \mathbf{\Phi}_s\, T_s^2/2 & \mathbf{\Phi}_s\, T_s \end{bmatrix}, \tag{68}$$

where T_s is the sampling period, and $\mathbf{\Phi}_s \in \mathbb{R}^{n\times n}$ is the power spectral density matrix of the continuous acceleration noise. Assuming the acceleration noise is independent and isotropic across joints, we set

$$\mathbf{\Phi}_s = \phi_s\, \mathbf{I}_n, \qquad \phi_s = 8 \text{ rad}^2/\text{s}^3, \tag{69}$$

a value selected through tuning the calibration sequences. This term absorbs unmodeled effects, such as joint friction variations and link flexibility.

Initial state covariance.

The initial error covariance is block-diagonal,

$$\mathbf{P}_0 = \begin{bmatrix} \sigma_{q,0}^2\, \mathbf{I}_n & \mathbf{0}_{n\times n} \\ \mathbf{0}_{n\times n} & \sigma_{\dot{q},0}^2\, \mathbf{I}_n \end{bmatrix}, \tag{70}$$

with $\sigma_{q,0}^2 = 0.01$ rad^2 and $\sigma_{\dot{q},0}^2 = 8$ rad^2/s^2. The small position variance reflects high confidence in the initial configuration, whereas the larger velocity variance accommodates the absence of any prior on $\dot{\mathbf{q}}$ at the filter start-up. The zero off-diagonal blocks encode the absence of prior cross-correlation between the positions and velocities.

Measurement noise covariance.

The measurement noise covariance $\mathbf{R} \in \mathbb{R}^{2n\times 2n}$ is estimated empirically from static calibration recordings. Raw marker coordinates are converted to metric units and expressed in the base-marker frame; subtracting the time-averaged mean of each marker yields a zero-mean error sequence $\mathbf{e}$, from which we compute the sample covariance $\mathbf{R} = \text{cov}(\mathbf{e})$. This procedure captures both the per-axis variance and cross-correlated noise structure of the Qualisys Miqus M3 tracking system in the steady state. Transient effects, such as occlusion-induced dropouts, were handled separately during the measurement-association stage. The implementation is provided as `findCameraNoise.m` in the supplementary code archive [49].

8 Experimental results

To validate the proposed modeling and estimation framework, the Extended Kalman Filter (EKF) was evaluated using a physical 10-link pendulum platform. The evaluation focused on state tracking accuracy, the impact of camera sampling rates on estimation stability, and the real-time computational efficiency of the closed-form dynamics.

8.1 Real-time computational efficiency

A critical advantage of the proposed explicit closed-form matrix dynamics and analytical Jacobian is their computational efficiency, as shown in Section 4. Fig. 9 shows the per-iteration execution time recorded on the dSPACE MicroAutoBox II at a sampling frequency of $F_s = 600$ Hz. The measurement spans the full EKF cycle over a 10s representative run: RK4 integration of the closed-form dynamics, propagation of the analytical Jacobian, and measurement update. The iteration time remained within a narrow band of 985–995 μs, with a mean of approximately 990 μs and a peak-to-peak jitter below 10 μs.

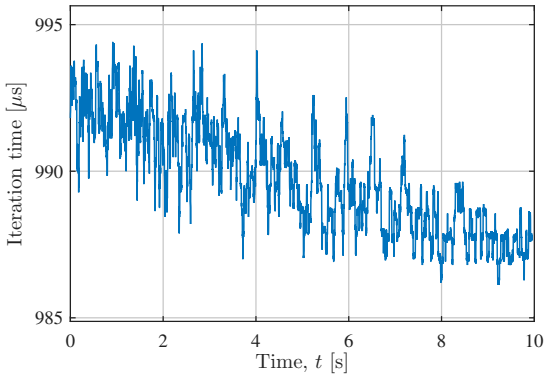


Fig. 9: Per-iteration EKF execution time on the dSPACE MicroAutoBox II at $F_s = 600$ Hz

Relative to the sampling period $T_s = 1/600$ s ≈ 1667 μs, these values correspond to the worst-case utilization of approximately 60%. This leaves a deterministic margin of approximately 670 μs per cycle, which is sufficient to absorb execution jitter without producing task overruns. No rising trend was observed across the 10s window. This confirms that the closed-form formulation does not exhibit state-dependent cost growth: the dominant operations — construction of $\mathbf{M}_0$, $\mathbf{C}_0$, and the structured Jacobian blocks — depend only on the diagonal sine/cosine matrices and the constant coupling matrix $\mathbf{W}$. Therefore, the per-iteration cost is governed by n alone rather than by the instantaneous configuration.

In contrast, when the iterative formulation of [2] was substituted into the same EKF skeleton, the per-iteration cost exceeded T_s. Sustained task overruns followed, rendering closed-loop execution at 600Hz infeasible. Fig. 9 thus provides the direct real-time counterpart to the offline timing benchmarks of Section 4.1.2 and demonstrates that, for $n \geq 10$, the closed-form approach is not an incremental optimization but a prerequisite for real-time state observation at this rate.

8.2 State tracking performance

Fig. 10 illustrates the time-domain trajectories of the measured and estimated joint angles ($\mathbf{q}$) and angular velocities ($\dot{\mathbf{q}}$) during an unforced tip-release experiment. The EKF, which was run at a baseline frequency of 600 Hz, successfully converged and accurately tracked the highly nonlinear and chaotic motion of the pendulum. Despite the presence of unmodeled joint flexibilities and sensor noise from the motion capture system, the filter maintained a stable estimate of the full 20-dimensional state vector throughout the transient and steady-state phases of motion.

To quantify estimation accuracy in a form that is comparable across states with different units and amplitudes, we report the per-state root-mean-square error (RMSE) and normalized RMSE (NRMSE), defined as

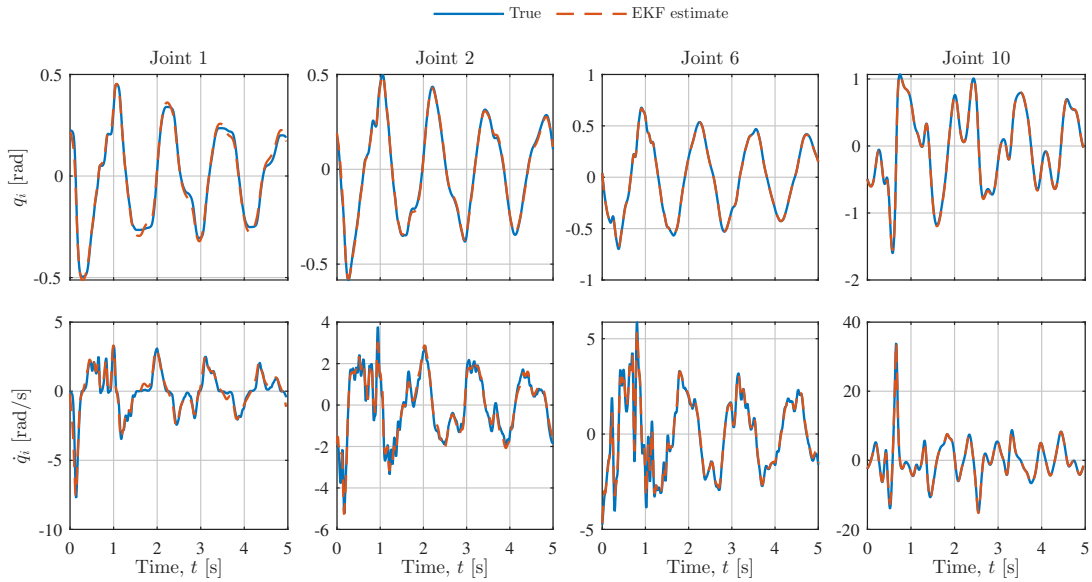
$$\mathrm{RMSE}_i = \sqrt{\frac{1}{N}\sum_{k=1}^{N}\left(x_{i,k} - \hat{x}_{i,k}\right)^2}, \tag{71}$$

$$\mathrm{NRMSE}_i = \frac{\mathrm{RMSE}_i}{\max\limits_k x_{i,k} \;-\; \min\limits_k x_{i,k}}, \tag{72}$$

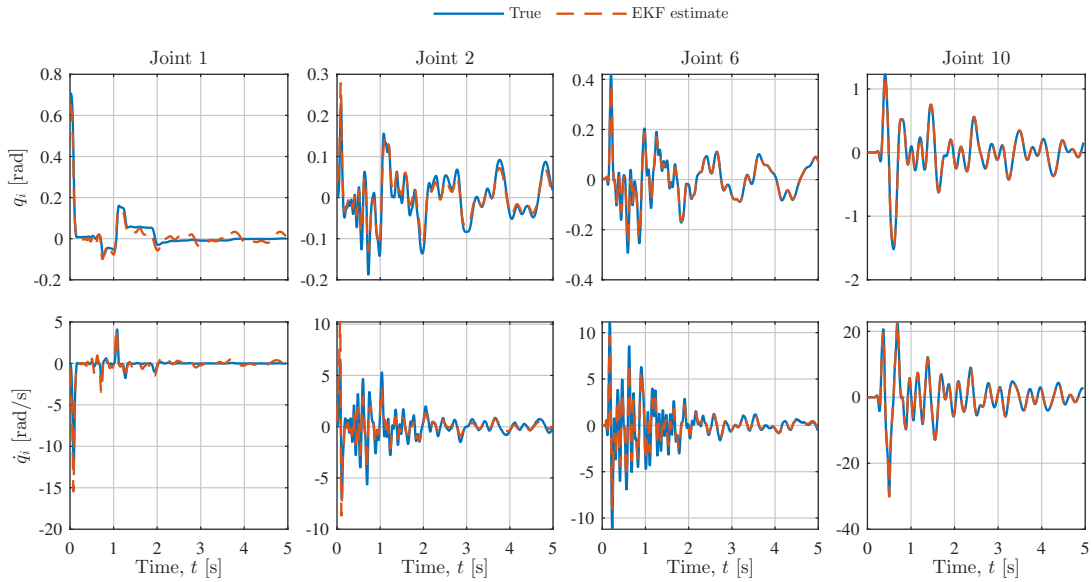
where $x_{i,k}$ and $\hat{x}_{i,k}$ denote the true and estimated i-th state at time step k, N is the number of samples, and the first n components of the state correspond to joint positions q while the The remaining n correspond to the joint velocities $\dot{q}$. The per-state range normalization in (72) removes both the unit mismatch between q (rad) and $\dot{q}$ (rad/s) and the per-joint amplitude bias, so that the resulting NRMSE is dimensionless and comparable across states. A single scalar score is then obtained by averaging across states,

$$\overline{\mathrm{NRMSE}} = \frac{1}{2n}\sum_{i=1}^{2n}\mathrm{NRMSE}_i. \tag{73}$$

The performance across all `long` and `base` trials is presented in Table 4.



(a) Tip-release experiment `(long, 600, 3)`



(b) Base-release experiment `(base, 600, 3)`

Fig. 10: Measured (solid) and EKF-estimated (dashed) joint angles $\mathbf{q}$ and angular velocities $\dot{\mathbf{q}}$ for representative joints $i \in \{1, 2, 6, 10\}$ of the 10-link pendulum at $F_s = 600$ Hz

8.3 Sampling rate sensitivity

Beyond the baseline 600Hz performance, we examined how the EKF tracking accuracy varied with the rate at which measurements were obtained. Fig. 11 shows three recorded experiments across every integer decimation factor of the 600 Hz camera stream, with the mean NRMSE computed using (73). Three regimes were observed.

For $F_s \gtrsim 10$ Hz, the curves saturate at a noise-and-model-mismatch floor of $\overline{\text{NRMSE}} \approx 10^{-2}$, consistent with the per-trial values reported

Table 4: Mean NRMSE (%) across trials at $F_s = 600$ Hz, averaged over position states $\mathbf{q}$, velocity states $\dot{\mathbf{q}}$, and all 2n states

	$\overline{\text{NRMSE}}$ (%)		
Type	q	$\dot{q}$	total
long	0.687 ± 0.206	1.902 ± 0.209	1.294 ± 0.188
base	1.254 ± 0.118	1.851 ± 0.298	1.553 ± 0.206

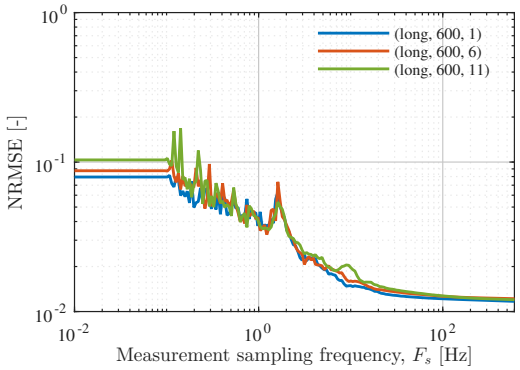


Fig. 11: Mean NRMSE across the state vector versus measurement sampling frequency, for three tip-release trials

in Table 4 and reflecting the irreducible camera noise and unmodeled-dynamics contributions, which the filter cannot remove regardless of the update rate. In the opposite extreme, $F_s \lesssim 10^{-1}$ Hz, the EKF operates almost exclusively in the prediction phase with insufficient measurement updates to correct the propagated state; the resulting $\overline{\text{NRMSE}} \approx 10^{-1}$ is consistent with the cumulative integration drift expected in a high-DOF nonlinear system over the 10 s recording.

Between these limits, the error generally decays with increasing correction frequency, but a prominent spike interrupts the otherwise monotonic trend near $F_s \approx 1.6$ Hz. Linearization of the 10-link pendulum about the stable equilibrium ($\mathbf{q} = \mathbf{0}, \dot{\mathbf{q}} = \mathbf{0}$) places the dominant fundamental mode at $f_1 = 0.7971$ Hz, so $F_s \approx 1.6$ Hz corresponds to approximately twice this frequency, which is the Nyquist rate of the dominant linearized mode. At this update rate, the measurements are aliased with respect to the dominant oscillation: successive innovations sample the dominant mode at nearly the same phase, the information they carry about that mode becomes nearly degenerate across updates, and the EKF effectively loses observability of the corresponding state directions. The covariance update is then driven by a poorly conditioned innovation sequence, and the resulting bias manifests as an observed NRMSE spike. Above this rate, additional measurement updates progressively restore the observability, and the error resumes a monotonic decay toward the noise floor.

9 Conclusion

This paper presents a unified framework for the modeling, chaos analysis, and real-time state estimation of n-link planar pendulum systems, organized around four contributions.

First, an explicit closed-form matrix representation of the n-link pendulum dynamics in absolute generalized coordinates was derived, in which the mass, Coriolis/centrifugal, and gravity terms were constructed from diagonal sine and cosine matrices and a constant coupling matrix $\mathbf{W} = \mathbf{\Lambda}^\top \mathbf{D}_m \mathbf{\Lambda}$. The skew-symmetry of $\dot{\mathbf{M}} - 2\mathbf{C}$ was established in closed form, ensuring that the Hamiltonian structure of the conservative system is preserved at the algebraic level rather than only numerically. Empirical benchmarking against a state-of-the-art iterative reference showed scaling of $t \propto n^{0.97}$ versus $n^{2.06}$ within the operating range $n \in [1, 40]$.

Second, the analytical continuous-time Jacobian of the full state transition is derived using the same structured operands as the dynamics. The formulation eliminates both the truncation error and the $\mathcal{O}(n)$ overhead of finite-difference linearization, and is validated against a central-difference reference, with the relative Frobenius-norm error reaching $\sim 6 \times 10^{-10}$ at the optimal step size for $n = 15$.

Third, the closed-form dynamics and analytical Jacobian enabled a systematic chaos analysis across $n = 1, \ldots, 12$, combining recurrence quantification with the full Benettin–QR Lyapunov spectrum. The Hamiltonian conjugate-pair symmetry and sum-to-zero property of the spectrum were recovered numerically across all link counts, providing independent confirmation of the analytical derivation. Three diagnostics — the longest diagonal $L_{\max}$, the determinism DET, and the leading exponents $\lambda_{\max}, \lambda_2$ — consistently identify

$n = 3$ as the principal transition into hyperchaos at the chosen energy fraction.

Fourth, the framework was validated on a custom-built 10-link experimental pendulum tracked at 600 Hz by a Qualisys motion-capture system. An Extended Kalman Filter using the analytical Jacobian recovered the full 20-dimensional state from Cartesian markers in real time on dSPACE MicroAutoBoxII hardware, with a per-iteration cost well below the sampling period and no state-dependent runtime growth. A sampling-rate sweep further revealed an observability collapse when the measurement rate approached the Nyquist rate of the dominant linearized mode, identifying a lower bound on the measurement frequency at which the EKF could track the system.

The present study has several limitations. The dynamics formulation is restricted to planar motion; extension to spatial n-link chains would require revisiting the kinematic matrix $\mathbf{\Lambda}$ and the diagonal sine/cosine matrices. Chaos analysis was performed on the conservative system, and friction was not included in the Lyapunov spectrum computation. The experimental validation was restricted to $n = 10$ and unforced motion. Finally, the EKF was evaluated against marker-derived ground truth rather than an independent angular sensor; an inertial cross-check at one or two joints would tighten the empirical claim.

Several directions extend naturally from this study. The structural properties exploited here — the constant coupling matrix, closed-form skew-symmetry, and analytical Jacobian construction — are expected to carry over to spatial n-link chains and to forced or controlled configurations, although the kinematic operands require revisiting. Introducing dissipation breaks the Hamiltonian pairing of the Lyapunov spectrum and replaces the transition to hyperchaos with a strange attractor whose dimension can be characterized by the same framework. Augmenting the present EKF with consistency diagnostics (NEES/NIS) across the sampling sweep and benchmarking against ensemble and particle filters at low measurement rates would provide a quantitative consistency benchmark for the sampling-rate guidelines reported in Section 8.2.

Declarations

- Funding: The authors declare that no funds, grants, or other support were received during the preparation of this manuscript.
- Competing interests: The authors have no relevant financial or non-financial interests to disclose.
- Data availability: The datasets generated during and/or analyzed during the current study are available in the Zenodo repository at https://doi.org/10.5281/zenodo.20303243.
- Author contribution: All authors contributed to the study conception and design. Simulations were performed by H.K. and Z.B., experimental data was collected by H.K., initial paper draft was written by H.K. Final paper was edited and corrected by Z.B. All authors read and approved the final manuscript.

Appendix A Proof of Eqs. (38) and (39)

Using Eq. (37) we can compute the partial derivative using a basic chain rule as

$$\begin{aligned}\frac{\partial \mathbf{M}_0}{\partial q_k} &= \frac{\partial \mathbf{D}_c}{\partial q_k}\mathbf{W}\mathbf{D}_c + \mathbf{D}_c\mathbf{W}\frac{\partial \mathbf{D}_c}{\partial q_k} \\ &\quad + \frac{\partial \mathbf{D}_s}{\partial q_k}\mathbf{W}\mathbf{D}_s + \mathbf{D}_s\mathbf{W}\frac{\partial \mathbf{D}_s}{\partial q_k} \\ &= -\mathbf{E}_k\mathbf{D}_s\mathbf{W}\mathbf{D}_c - \mathbf{D}_c\mathbf{W}\mathbf{E}_k\mathbf{D}_s \\ &\quad + \mathbf{E}_k\mathbf{D}_c\mathbf{W}\mathbf{D}_s + \mathbf{D}_s\mathbf{W}\mathbf{E}_k\mathbf{D}_c \end{aligned} \tag{A1}$$

For an arbitrary diagonal matrix $\mathbf{U}$, the matrices $\mathbf{E}_k$ and $\mathbf{U}$ commute, hence we can write $\mathbf{E}_k$ on the right side of the matrix products in Eq. (A1) as

$$\begin{aligned}\frac{\partial \mathbf{M}_0}{\partial q_k} &= (\mathbf{D}_s\mathbf{W}\mathbf{D}_c - \mathbf{D}_c\mathbf{W}\mathbf{D}_s)\mathbf{E}_k \\ &\quad - \mathbf{E}_k(\mathbf{D}_s\mathbf{W}\mathbf{D}_c - \mathbf{D}_c\mathbf{W}\mathbf{D}_s) \\ &= \mathbf{C}_0\mathbf{E}_k - \mathbf{E}_k\mathbf{C}_0 \end{aligned} \tag{A2}$$

The same procedure can be followed for $\frac{\partial \mathbf{C}_0}{\partial q_k}$

$$\begin{aligned}\frac{\partial \mathbf{C}_0}{\partial q_k} &= \frac{\partial \mathbf{D}_s}{\partial q_k}\mathbf{W}\mathbf{D}_c + \mathbf{D}_s\mathbf{W}\frac{\partial \mathbf{D}_c}{\partial q_k} \\ &\quad - \frac{\partial \mathbf{D}_c}{\partial q_k}\mathbf{W}\mathbf{D}_s - \mathbf{D}_c\mathbf{W}\frac{\partial \mathbf{D}_s}{\partial q_k}\end{aligned}$$

$$= \mathbf{E}_k\mathbf{D}_c\mathbf{W}\mathbf{D}_c - \mathbf{D}_s\mathbf{W}\mathbf{E}_k\mathbf{D}_s + \mathbf{E}_k\mathbf{D}_s\mathbf{W}\mathbf{D}_s - \mathbf{D}_c\mathbf{W}\mathbf{E}_k\mathbf{D}_c \quad \text{(A3)}$$

$$\frac{\partial \mathbf{C}_0}{\partial q_k} = -(\mathbf{D}_c\mathbf{W}\mathbf{D}_c + \mathbf{D}_s\mathbf{W}\mathbf{D}_s)\mathbf{E}_k + \mathbf{E}_k(\mathbf{D}_c\mathbf{W}\mathbf{D}_c + \mathbf{D}_s\mathbf{W}\mathbf{D}_s) = -\mathbf{M}_0\mathbf{E}_k + \mathbf{E}_k\mathbf{M}_0 \quad \text{(A4)}$$

References

[1] Hazem, Z.B., Bingül, Z.: Comprehensive Review of Different Pendulum Structures in Engineering Applications. IEEE Access **11**, 42862–42880 (2023) https://doi.org/10.1109/ACCESS.2023.3269580

[2] Serkibayev, D., Zhakatayev, A., Rogovchenko, Y.: Dynamic equations for an n-link planar pendulum in absolute and relative coordinate systems and computational efficiency. Nonlinear Dynamics **114**(1), 19 (2026) https://doi.org/10.1007/s11071-025-11862-1

[3] Zhang, S., He, X., Zhu, H.: Barrier function-based adaptive antisway control for underactuated overhead cranes. Nonlinear Dynamics **111**(19), 18077–18093 (2023) https://doi.org/10.1007/s11071-023-08803-1

[4] Xin, X., Pan, J., Xu, B.: Coupling-Energy-Based Antiswing PD Control for a General n -Link Pendulum–Cart System: Theory and Experimental Validation. IEEE Transactions on Industrial Electronics **72**(6), 6194–6204 (2025) https://doi.org/10.1109/TIE.2024.3497297

[5] Glück, T., Eder, A., Kugi, A.: Swing-up control of a triple pendulum on a cart with experimental validation. Automatica **49**(3), 801–808 (2013) https://doi.org/10.1016/j.automatica.2012.12.006

[6] Jahn, B., Watermann, L., Reger, J.: On the design of stable periodic orbits of a triple pendulum on a cart with experimental validation. Automatica **125**, 109403 (2021) https://doi.org/10.1016/j.automatica.2020.109403

[7] Chikmagalur, K., Bamieh, B.: Vibrational stabilization of multi-link mechanical systems. Automatica **165**, 111589 (2024) https://doi.org/10.1016/j.automatica.2024.111589

[8] Konigsmarkova, J., Schlegel, M.: Identification of n-link inverted pendulum on a cart. In: 2017 21st International Conference on Process Control (PC), pp. 42–47. IEEE, Strbske Pleso, Slovakia (2017). https://doi.org/10.1109/PC.2017.7976186

[9] Anan'evskii, I.M., Anokhin, N.V.: Control of the spatial motion of a multilink inverted pendulum using a torque applied to the first link. Journal of Applied Mathematics and Mechanics **78**(6), 543–550 (2014) https://doi.org/10.1016/j.jappmathmech.2015.04.001

[10] Manita, L.A., Ronzhina, M.I.: Optimal Synthesis in the Control Problem of an n-Link Inverted Pendulum with a Moving Base. Journal of Mathematical Sciences **221**(1), 137–153 (2017) https://doi.org/10.1007/s10958-017-3222-x

[11] Yesilyurt, B.: Equations of Motion Formulation of a Pendulum Containing N-point Masses. arXiv. Version Number: 2 (2019). https://doi.org/10.48550/ARXIV.1910.12610

[12] Karhan, H., Bingül, Z.: Automatic Determination of the Denavit–Hartenberg Parameters for the Forward Kinematics of All Serial Robots: Novel Kinematics Toolbox. Machines **13**(10), 944 (2025) https://doi.org/10.3390/machines13100944

[13] Lee, T., Leok, M., McClamroch, N.H.: Dynamics and Control of a Chain Pendulum on a Cart. arXiv. Version Number: 1 (2012). https://doi.org/10.48550/ARXIV.1211.4604

[14] Das, S., Patil, D.: Disturbance Decoupling Problem for n-link chain pendulum on a cart system. arXiv. Version Number: 1 (2024). https://doi.org/10.48550/ARXIV.2402.19168 . https://arxiv.org/abs/2402.19168

[15] Morozumi, D., Sumioka, T., Shin, H.: Energy-Based Closed-Form Solution of the Divergent Component of Motion for Nonlinear Inverted Pendulum Trajectories. IEEE Robotics and Automation Letters **11**(3), 2754–2761 (2026) https://doi.org/10.1109/LRA.2026.3654449

[16] Kocbay, E.: Asymptotics on the dynamics of the hanging chain pendulum. Meccanica **61**(1), 18 (2026) https://doi.org/10.1007/s11012-025-02075-2

[17] Disca, S., Coscia, V.: Chaotic dynamics of a continuous and discrete generalized Ziegler pendulum. Meccanica **59**(7), 1139–1157 (2024) https://doi.org/10.1007/s11012-024-01848-5

[18] Udwadia, F.E., Koganti, P.B.: Dynamics and control of a multi-body planar pendulum. Nonlinear Dynamics **81**(1-2), 845–866 (2015) https://doi.org/10.1007/s11071-015-2034-0

[19] Anurag, Das, A., Chakraborty, S.: Order and chaos around resonant motion in librating spring–mass–spherical pendulum. Nonlinear Dynamics **104**(4), 3407–3424 (2021) https://doi.org/10.1007/s11071-021-06455-7

[20] Abohamer, M.K., Amer, T.S., Abdelhfeez, S.A., Eldawoody, D.A., Elbaz, R.F.: Vibration analysis, stability assessment, and chaotic behavior of a damped oscillator coupled with a spherical pendulum and a piezoelectric transducer. Nonlinear Dynamics **113**(18), 24343–24381 (2025) https://doi.org/10.1007/s11071-025-11395-7

[21] Amer, T.S., El-Sabaa, F.M., Zakria, S.K., Galal, A.A.: The stability of 3-DOF triple-rigid-body pendulum system near resonances. Nonlinear Dynamics **110**(2), 1339–1371 (2022) https://doi.org/10.1007/s11071-022-07722-x

[22] Amer, T.S., Moatimid, G.M., Zakria, S.K., Galal, A.A.: Vibrational and stability analysis of planar double pendulum dynamics near resonance. Nonlinear Dynamics **112**(24), 21667–21699 (2024) https://doi.org/10.1007/s11071-024-10169-x

[23] Stachowiak, T., Okada, T.: A numerical analysis of chaos in the double pendulum. Chaos, Solitons & Fractals **29**(2), 417–422 (2006) https://doi.org/10.1016/j.chaos.2005.08.032

[24] Dudkowski, D., Wojewoda, J., Czołczyński, K., Kapitaniak, T.: Is it really chaos? The complexity of transient dynamics of double pendula. Nonlinear Dynamics **102**(2), 759–770 (2020) https://doi.org/10.1007/s11071-020-05697-1

[25] Luo, A.C.J., Guo, Y.: Periodic Motions to Chaos in Pendulum. International Journal of Bifurcation and Chaos **26**(09), 1650159 (2016) https://doi.org/10.1142/S0218127416501595

[26] Benettin, G., Galgani, L., Giorgilli, A., Strelcyn, J.-M.: Lyapunov Characteristic Exponents for smooth dynamical systems and for hamiltonian systems; a method for computing all of them. Part 1: Theory. Meccanica **15**(1), 9–20 (1980) https://doi.org/10.1007/BF02128236

[27] Benettin, G., Galgani, L., Giorgilli, A., Strelcyn, J.-M.: Lyapunov Characteristic Exponents for smooth dynamical systems and for hamiltonian systems; A method for computing all of them. Part 2: Numerical application. Meccanica **15**(1), 21–30 (1980) https://doi.org/10.1007/BF02128237

[28] Skokos, C.: The Lyapunov Characteristic Exponents and Their Computation. In: Souchay, J.J., Dvorak, R. (eds.) Dynamics of Small Solar System Bodies and Exoplanets vol. 790, pp. 63–135. Springer, Berlin, Heidelberg (2010). https://doi.org/10.1007/978-3-642-04458-8_2

[29] Wolf, A., Swift, J.B., Swinney, H.L., Vastano, J.A.: Determining Lyapunov exponents from a time series. Physica D: Nonlinear Phenomena **16**(3), 285–317 (1985) https://doi.org/10.1016/0167-2789(85)90011-9

[30] Rosenstein, M.T., Collins, J.J., De Luca, C.J.: A practical method for calculating largest Lyapunov exponents from small data

sets. Physica D: Nonlinear Phenomena **65**(1-2), 117–134 (1993) https://doi.org/10.1016/0167-2789(93)90009-P

[31] Yang, C., Wu, Q.: On stability analysis via Lyapunov exponents calculated from a time series using nonlinear mapping—a case study. Nonlinear Dynamics **59**(1-2), 239–257 (2010) https://doi.org/10.1007/s11071-009-9535-7

[32] Yang, C., Wu, C.Q., Zhang, P.: Estimation of Lyapunov exponents from a time series for n-dimensional state space using nonlinear mapping. Nonlinear Dynamics **69**(4), 1493–1507 (2012) https://doi.org/10.1007/s11071-012-0364-8

[33] Balcerzak, M., Dabrowski, A., Pikunov, D.: Tuning the control system of a nonlinear inverted pendulum by means of the new method of Lyapunov exponents estimation, Lublin, Poland, p. 100016 (2018). https://doi.org/10.1063/1.5019101 . https://pubs.aip.org/aip/acp/article/608330

[34] Balcerzak, M., Pikunov, D., Dabrowski, A.: The fastest, simplified method of Lyapunov exponents spectrum estimation for continuous-time dynamical systems. Nonlinear Dynamics **94**(4), 3053–3065 (2018) https://doi.org/10.1007/s11071-018-4544-z

[35] Ting, J., Marghitu, D.B.: Analyzing Double Pendulum Dynamics with Approximate Entropy and Maximal Lyapunov Exponent. In: Dumitru, I., Matei, L., Racila, L.D., Rosca, A.S. (eds.) Proceedings of the International Conference on Mechanical Engineering (ICOME 2022) vol. 15, pp. 167–174. Atlantis Press International BV, Dordrecht (2023). https://doi.org/10.2991/978-94-6463-152-4_19

[36] Marwan, N., Carmen Romano, M., Thiel, M., Kurths, J.: Recurrence plots for the analysis of complex systems. Physics Reports **438**(5-6), 237–329 (2007) https://doi.org/10.1016/j.physrep.2006.11.001

[37] Duarte, L.G.S., Da Mota, L.A.C.P., De Oliveira, H.P., Ramos, R.O., Skea, J.E.F.: Numerical analysis of dynamical systems and the fractal dimension of boundaries. Computer Physics Communications **119**(2-3), 256–271 (1999) https://doi.org/10.1016/S0010-4655(99)00204-0

[38] Litak, G., Wiercigroch, M., Horton, B.W., Xu, X.: Transient chaotic behaviour versus periodic motion of a parametric pendulum by recurrence plots. ZAMM - Journal of Applied Mathematics and Mechanics / Zeitschrift für Angewandte Mathematik und Mechanik **90**(1), 33–41 (2010) https://doi.org/10.1002/zamm.200900290

[39] Kwuimy, C.A.K., Samadani, M., Nataraj, C.: Bifurcation analysis of a nonlinear pendulum using recurrence and statistical methods: applications to fault diagnostics. Nonlinear Dynamics **76**(4), 1963–1975 (2014) https://doi.org/10.1007/s11071-014-1261-0

[40] Gupta, M.K., Sharma, P., Mondal, A., Kumar, A.: Visual Recurrence Analysis of Chaotic and Regular Motion of a Multiple Pendulum System. Arabian Journal for Science and Engineering **42**(7), 2711–2716 (2017) https://doi.org/10.1007/s13369-016-2342-9

[41] Jauregui-Correa, J.C.: Identification of Nonlinearities in Mechanical Systems Using Recurrence Plots. In: Jauregui, J.C. (ed.) Nonlinear Structural Dynamics and Damping vol. 69, pp. 83–118. Springer, Cham (2019). https://doi.org/10.1007/978-3-030-13317-7_4

[42] Van Der Veken, T., Croes, J., Kirchner, M., Baake, J., Desmet, W., Naets, F.: Exploiting Cyclic Angle-Dependency in a Kalman Filter-Based Torque Estimation on a Mechatronic Drivetrain. Actuators **11**(2), 35 (2022) https://doi.org/10.3390/act11020035

[43] Yin, Y., Yang, Q., Fang, H.: Error-State Kalman Filter Based External Wrench Estimation for MAVs Under a Cascaded Architecture. In: 2023 IEEE/RSJ International Conference on Intelligent Robots and Systems (IROS), pp. 5019–5026. IEEE, Detroit, MI, USA (2023). https://doi.org/10.1109/

IROS55552.2023.10342358

[44] Bagala, F., Fuschillo, V.L., Chiari, L., Cappello, A.: Calibrated 2D Angular Kinematics by Single-Axis Accelerometers: From Inverted Pendulum to ${\rm N}$-Link Chain. IEEE Sensors Journal **12**(3), 479–486 (2012) https://doi.org/10.1109/JSEN.2011.2107897

[45] Woods, C., Vikas, V.: Joint Angle Estimation Using Accelerometer Arrays and Model-Based Filtering. IEEE Sensors Journal **22**(20), 19786–19796 (2022) https://doi.org/10.1109/JSEN.2022.3200251

[46] Cervantes-Pérez, L., Santibáñez, V., Sandoval, J., Ortega, R., Romero, J.G.: An Experimental Comparison of Sliding Mode and Immersion and Invariance Adaptive Controllers forPosition-feedback Tracking of a Simple Mechanical System with Friction. arXiv. arXiv:2601.12545 [eess] (2026). https://doi.org/10.48550/arXiv.2601.12545

[47] Karhan, H.K., Bingul, Z.: Camera-based Online Torque Estimation of a Multi-link Pendulum via Extended Kalman Filtering. In: IECON 2025 – 51st Annual Conference of the IEEE Industrial Electronics Society, pp. 1–6. IEEE, Madrid, Spain (2025). https://doi.org/10.1109/IECON58223.2025.11221661

[48] Datseris, G.: DynamicalSystems.jl: A Julia software library for chaos and nonlinear dynamics. Journal of Open Source Software **3**(23), 598 (2018) https://doi.org/10.21105/joss.00598 . Accessed 2026-05-20

[49] Karhan, H., Bingül, Z.: Software for "Closed-form Matrix Dynamics of the N-link Pendulum: Chaos Analysis and Real-time State Estimation". https://doi.org/10.5281/zenodo.20303243